Measurement of the Double Beta Decay Half-life of Nd-150 with the NEMO-3 Experiment

---

A dissertation submitted to the University of Manchester for the degree of Master of Science in the Faculty of Engineering and Physical Sciences

MSc Thesis By Research

October 2012

William Poynter

High Energy Physics Group
School of Physics and Astronomy
University of Manchester

Contents

Abstract

Neodymium-150 (Nd-150) is analysed using a sample with a mass of 37 g within the NEMO-3 detector. In total, 4.42 years of data are analysed which yield a half-life for the double β decay of Nd-150 of

$$T_{1/2} = \left(8.55 \pm 0.18(stat.) \pm 0.39(syst.)\right) \times 10^{18} \text{ years.}$$

This includes the use of an updated background understanding and correction factors to remove biases introduced by coincidence and dead-time. The result is in agreement with the half-life previously determined using NEMO-3 data.

Declaration

No portion of the work referred to in this dissertation has been submitted in support of an application for another degree or qualification of this or any other university or other institute of learning.

The author of this thesis (including any appendices and/or schedules to this thesis) owns certain copyright or related rights in it (the "Copyright") and he has given The University of Manchester certain rights to use such Copyright, including for administrative purposes. Copies of this thesis, either in full or in extracts and whether in hard or electronic copy, may be made only in accordance with the Copyright, Designs and Patents Act 1988 (as amended) and regulations issued under it or, where appropriate, in accordance with licensing agreements which the University has from time to time. This page must form part of any such copies made. The ownership of certain Copyright, patents, designs, trade marks and other intellectual property (the "Intellectual Property") and any reproductions of copyright works in the thesis, for example graphs and tables ("Reproductions"), which may be described in this thesis, may not be owned by the author and may be owned by third parties. Such Intellectual Property and Reproductions cannot and must not be made available for use without the prior written permission of the owner(s) of the relevant Intellectual Property and/or Re- productions. Further information on the conditions under which disclosure, publication and commercialisation of this thesis, the Copyright and any Intellectual Property and/or Reproductions described in it may take place is avail- able in the University IP Policy (see http://www.campus.manchester.ac.uk/ medialibrary/policies/intellectual-property.pdf), in any relevant Thesis restriction declarations deposited in the University Library, The University Library regulations (see http://www.manchester.ac.uk/library/aboutus/ regulations) and in The University policy on presentation of Theses.

Acknowledgements

Firstly, I would like to thank my supervisor Stefan Söldner- Rembold for his guidance, patience and support over the past year. His wide knowledge and encouragement have been of great value for me. I would also like to thank Emmanuel Chauveau. This dissertation would not have been possible without his great amount of assistance and advice.

I am grateful to Stefano Torre and Anastasia Basharina-Freshville for their invaluable assistance using NEMO-3 software and all the members of NEMO-3 for detailed and constructive comments on my work. Thanks to Tom Bird for his endless tutorials on the use of Linux and Root, and to all the members of the Manchester Particle Physics group who made my time as a postgraduate student so special and enjoyable.

And last but not least, I would like to thank Lydia Lowry and my family for their continuous, and forever patient, support and encouragement, which made this year possible.

Chapter 1: Introduction

This thesis discusses the two-neutrino double β decay of Neodymium-150. The purpose of investigating this decay is to improve the understanding of the neutrino. Ever since the hypothesis of the neutrino by Pauli in 1930 there have been great mysteries about its properties. Pauli deduced the existence of a second particle emitted by β decay in order to explain the energy spectrum observed.[1] In 1956, Cowan & Reines experimentally established the existence of the neutrino.[2]

After confirming the existence of the neutrino it was, and continues to be, necessary to measure and understand its properties. This has led to many experiments attempting to measure the mass of the neutrino with no conclusive result. However, these experiments have led to the discovery of other neutrino properties that were not initially hypothesised.

Observations of solar neutrinos led to a problem whereby approximately only one third of the hypothesised flux of neutrinos was being detected.[3] It was at this point that the theory that neutrinos are able to oscillate between lepton flavours was advanced. The Sudbury Neutrino Observatory (SNO) confirmed this theory by showing that neutrinos were able to violate lepton flavour conservation by a process that is disallowed for the

charged leptons.[4] The ability for neutrinos to oscillate between flavours is highly relevant as this process requires neutrinos to have mass. One of the key reasons for measuring double β decay is to measure the mass of the neutrino. The measurement of two-neutrino double β decay (2νββ) is important as it is a irreducible background of neutrinoless double β decay (0νββ), which is a vital probe in searching for Majorana neutrinos. The discovery of Majorana neutrinos would provide conclusive evidence of lepton number violation.[5] NEMO-3 aims to investigate these properties of the neutrino using multiple isotopes, including Neodenium-150, which is discussed and analysed within this thesis.

Chapter 2: Theory

2.1 Neutrino Mass in the Standard Model

Within the Standard Model (SM), neutrinos are massless Dirac fermions, which do not gain mass through the Higgs mechanism, unlike the charged leptons.[6] Neutrinos carry lepton number, which under the SM must be conserved for any physics process. The NEMO-3 experiment was constructed to test this characteristic of neutrinos via the process of neutrinoless double β decay.

Neutrinoless double β decay, if discovered, will be the rarest nuclear decay process and its existence will demonstrate physics beyond the Standard Model, as lepton number will be violated. It would also mean that the neutrino is the first Majorana fermion, which could lead to an exciting new range of physics.[7]

The aforementioned discovery of neutrino flavour mixing is described by a model where the neutrinos have three mass eigenstates (ν_1, ν_2, ν_3), different from the flavour eigenstates (ν_e,ν_μ,ν_τ). The existence of these different eigenstates leads to flavour oscillations.[8]

(2.2)

(2.1)

(2.3)

2.3 PMNS Matrix

The Pontecorvo-Maki-Nakagawa-Sakata (PMNS) matrix is used to describe the mixing relationship between the flavour and mass eigenstates, just as the Cabbibo- Kobayashi–Maskawa (CKM) matrix is used for quarks. It is given by the relation

$$\begin{pmatrix} \nu_e \\ \nu_\mu \\ \nu_\tau \end{pmatrix} = \begin{pmatrix} U_{e1} & U_{e2} & U_{e3} \\ U_{\mu 1} & U_{\mu 2} & U_{\mu 3} \\ U_{\tau 1} & U_{\tau 2} & U_{\tau 3} \end{pmatrix} \begin{pmatrix} \nu_1 \\ \nu_2 \\ \nu_3 \end{pmatrix}$$

where U_{ij} is proportional to the probability of a neutrino of flavour i, being observed at mass state j. As the PMNS matrix is a unitary matrix it can be written in terms of the Dirac phase and mixing angles,

$$U_{\alpha i} = \begin{pmatrix} c_{12} & s_{12} & 0 \\ -s_{12} & c_{12} & 0 \\ 0 & 0 & 1 \end{pmatrix} \begin{pmatrix} 1 & 0 & 0 \\ 0 & c_{23} & s_{23} \\ 0 & -s_{23} & c_{23} \end{pmatrix} \begin{pmatrix} c_{13} & 0 & s_{13}e^{-i\delta} \\ 0 & 1 & 0 \\ -s_{13}e^{i\delta} & 0 & c_{13} \end{pmatrix} \begin{pmatrix} 1 & 0 & 0 \\ 0 & e^{\phi_1} & 0 \\ 0 & 0 & e^{\phi_2} \end{pmatrix}$$

where ϕ_n are the Majorana phase angles, s_{ij} and c_{ij} are the sine and cosine of the mixing angle θ_{ij} respectively and δ represents Dirac phase, which indicates CP-violation.[9]

2.4 The Mass Scale Problem

The probability of a neutrino oscillating between one flavour and another is related to the separation between the different mass eigenstates squared.

$$\Delta m_{ij}^2 = m_i^2 - m_j^2$$

Many observations have led to the development of two key mass hierarchies that describe the distribution of the mass eigenstates. Both the 'Normal' and 'Inverted' mass hierarchies describe a small mass difference between m_1 and m_2, but a larger separation to m_3 (Figure 1). Although it is possible to determine the relative separation of the mass

eigenstates, it is not possible to predict the absolute mass values of m_1, m_2 and m_3 from oscillation measurements, and therefore the absolute mass scale must be measured directly using several different processes, in which double β decay is one of the most promising.[10] (2.4)

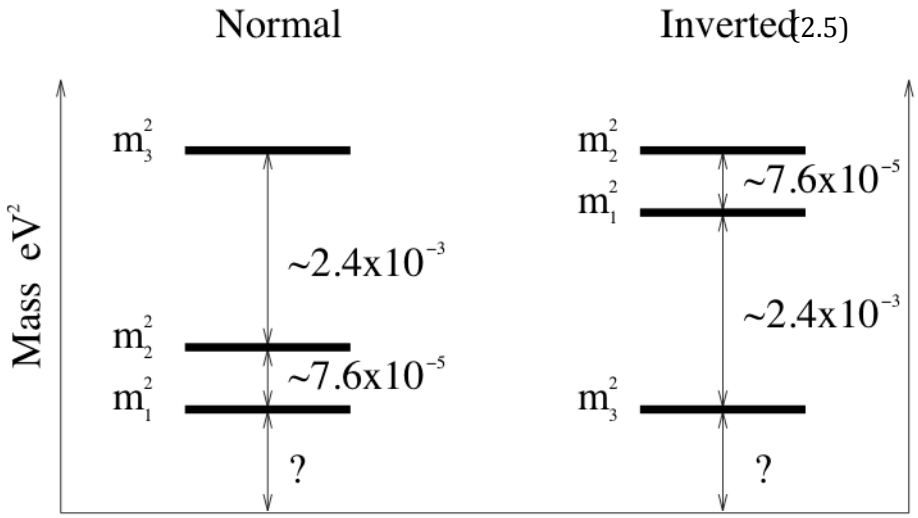

(2.5)

Figure 1 - The 'Normal' and 'Inverted' mass hierarchies of the neutrino mass states are illustrated on the left and right, respectively.[11]

2.5 Double Beta Decay

Double-β decay is currently the rarest nuclear decay process observed. Theoretically there are 35 naturally occurring isotopes that are able to decay via double β decay, of which 12 have so far been observed to decay. In these cases standard β decay is forbidden by energy or angular momentum conservation, however it is not forbidden for it to undergo two simultaneous β decays.

$$(A,Z) \Rightarrow (A,Z+1) + e^- + \overline{\upsilon_e}$$

$$(A,Z) \Rightarrow (A,Z+2) + 2e^- + 2\overline{\upsilon_e}$$

It has been hypothesised that is possible to observe a process of double β decay that does not produce any neutrinos, dubbed neutrinoless double β decay, which requires

the neutrino to be a Majorana particle.[12] The two types of double β decay are shown in Figure 2.

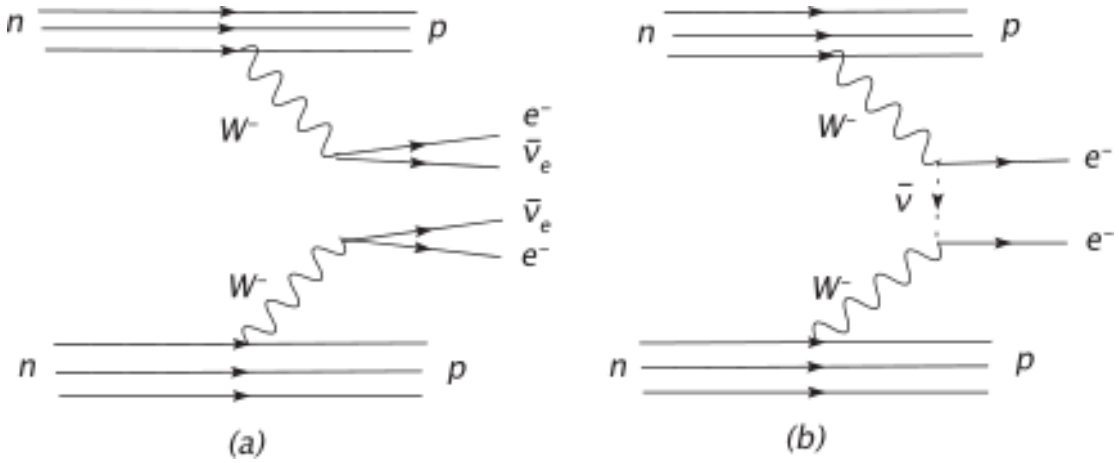

Figure 2 - Feynman diagrams of 2νββ decay (a) and 0νββ decay (b).[13]

Chapter 3: The NEMO-3 Detector

The NEMO-3 detector is located at the Modane Underground Laboratory under the Col de Fréjus, on the Franco-Italian border. The detector is designed to measure double β decay processes in multiple isotopes simultaneously.

Typically double β decay experiments can be divided into two categories: those where the active material makes up a part of the detector itself are called homogenous, and those where the detector is split into several components are called heterogeneous; the NEMO-3 detector is of the latter type.

In total the NEMO-3 detector has a mass of 200,000 kg and is a cylinder of 4 m high and 6 m in diameter. A photograph from the installation of the detector is shown in Figure 3.The entire detector is split into twenty sectors labelled 0 to 19, each one being a segment with an opening angle of 18°. Each of these segments consists of 7 source strips positioned in the centre. Cladding the foils, on either side, are the tracker modules, which are used to identify type, charge and vertex of the particle. Outside of the trackers are the calorimeters, which measures the energy of incident particles.[14]

The centre of the detector in every dimensionless is marked as the origin for the coordinate system. The Z-axis describes the vertical height, and ϕ denotes the rotation from the beginning of Sector 0, increasingly to Sector 19.

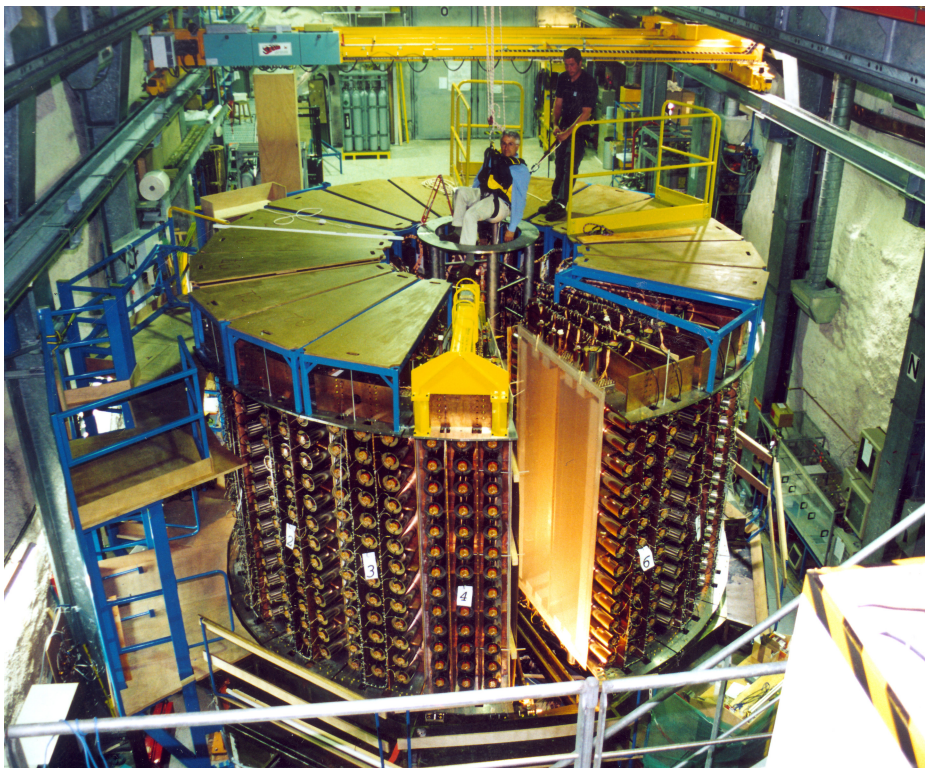

Figure 3 - The NEMO-3 detector under construction within the Underground Modane Laboratory.

3.1 Source Foils

Each sector is able to hold seven strips at a radius of 1549 mm from the centre of the detector. Each strip is typically 2500 mm long and 65 mm wide with an area density of 30-60 mg cm^{-2} and holds a single source foil. This configuration of source foils allows the NEMO-3 experiment to investigate seven separate double β isotopes. The range of isotopes used, their mass, and their Q(ββ) are shown in Table 1.

Isotope	Mass / g	Q(ββ) / MeV
^{100}Mo	6914	3.034
^{82}Se	932	2.995
^{130}Te	454	2.529
^{116}Cd	405	2.805
^{150}Nd	36.5	3.367
^{96}Zr	9.4	3.350
^{48}Ca	7.0	4.272

Table 1 - The double βdecay source isotopes of the NEMO-3 experiment including the mass used and the Q(ββ) of the respective isotopes.[14]

A photograph of a source foil strip from the installation phase is shown in Figure 4.

3.1.1 The Neodymium Foil

The Nd-150 foil is a composite foil of Nd_2O_3, which is positioned in Strip 6, Sector 5, of the detector between 1.802 and 1.845 radians in phi and -117 cm and 117 cm in the Z coordinate. The total mass of the foil is 57 g and it is enriched to 95±0.5%, in which 36.5±0.1 g is Nd-150. Of the total mass of the foil 6.458 g is provided by the Mylar support film that gives the foil its structure. Using a high purity Germanium (HPGe) detector the main radioactive impurities of the foil are determined to be Pa-234m, Bi-207, Eu-154, Eu-152, Bi-214, Pb-214, Tl-208 and K-40.

In addition to the homogenous impurities detected, distributed evenly over the foil, there is a Pa-234m heterogeneous contamination (hotspots) of high activity.[15]

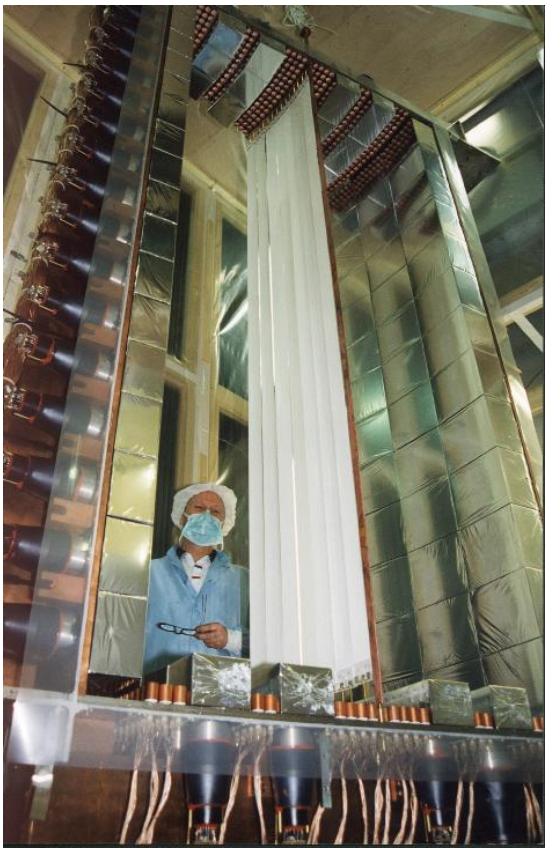

Figure 4 - The commissioning of a sector of the NEMO-3 detector including source strips without tracking Geiger cells.

3.2 The Tracker

The tracking of charged particles through the detector is performed by 6180 Geiger cells, which are composed of 39,820 vertical drift wires. Each cell is 3 cm in diameter and consists of a single central wire and eight surrounding ground wires. The cells are distributed in a 4-2-3 configuration going away from the source foils on either side. An additional guard wire separated the layers of cells in order to reduce electromagnetic interference between successive layers. All of the wires have a diameter of 50 μm and are made of stainless steel. The anode wires carry around 1620 V with a maximum voltage of 1900 V. A schematic view of the tracking detector is shown in Figure 5.

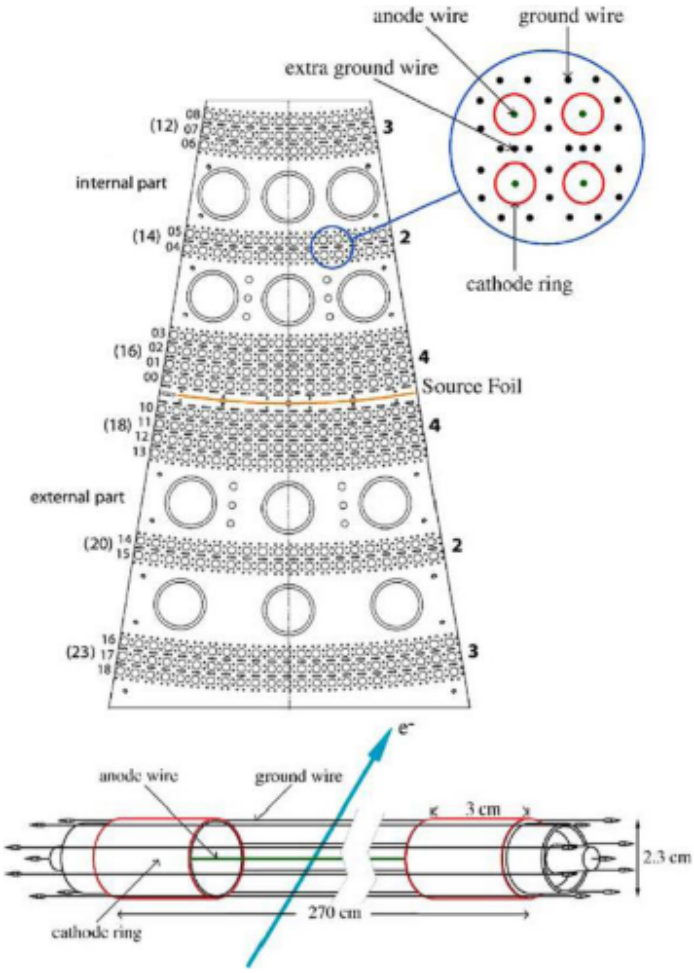

Figure 5 - An aerial schematic view of a single section of the NEMO-3 detector, demonstrating the distribution of the Geiger cells (top). A schematic view of the cross-section of a single Geiger cell (bottom).

At the ends of each cell a cylindrical copper tube is positioned, which is 3 cm long and 2.3 cm in diameter. The anode wire runs through the centre of the cylinder.

The gaseous volume of the Geiger cells comprises a mixture of helium, ethyl alcohol, argon and water. Helium is chosen for its low atomic number thus minimising energy loss and multiple scattering of charged particles passing through the gas. Ethyl alcohol is used as a quencher limiting the production of UV γ and therefore avalanches. During commissioning of the detector in 2003, Argon and water were added to the mixture, in the proportions of 1% and 1500 ppm respectively, in order to reduce noise and increase cell stability. There was also a known infiltration of radon gas into the gas mixture of the detector.

The entire tracker is subjected to a 25 Gauss field in order to curve charged particles, enabling discrimination between charges.[14]

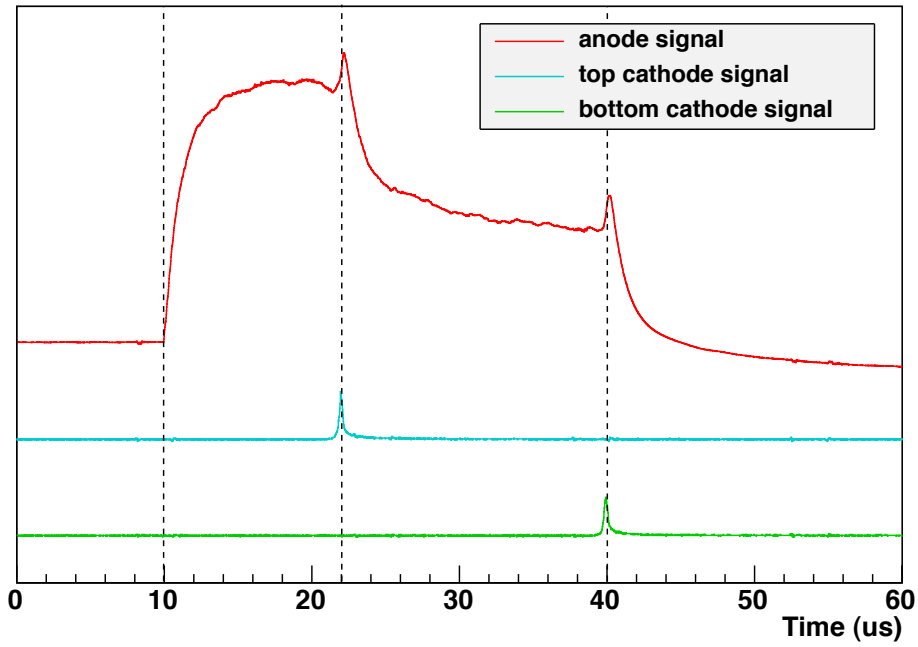

Figure 6 - The three response signals from a single Geiger detection. The anode signal denotes the arrival of the plasma to the anode wire at 10 µs. The cathode signals denote the arrival of the plasma at the top and bottom of the cell respectively.

Upon a charged particle entering the Geiger cell, the gas is ionised and a cascade of electrons forms a plasma that propagates towards the two ends of the Geiger cell.

In order for the Geiger cells to accurately determine the position that a particle interacts with the cell, three time measurements are required. The pulse structure is shown in Figure 6. The first is the time difference between the particle entering the cell and the plasma reaching the anode wire; this gives the radius of the particle trajectory from the centre of the cell. Upon the plasma propagating to the two cathode rings at either end of the cells a signal is received. Using the two cathode signals, it is possible to obtain the Z position of the interaction along the length of the cell.[14]

3.3 The Calorimeter

In order to measure the energy and time-of-flight (TOF) of a particle within the NEMO-3 experiment, four walls of calorimeter are used. The calorimeter consists of 1940 scintillator blocks attached to a combination of 3” or 5” photomultiplier tubes (PMTs) via the use of a light guide. The four walls of scintillators are referred to as internal, external, top and bottom encompassing a rectangular-ended toroidal volume. A schematic view is shown in Figure 7.

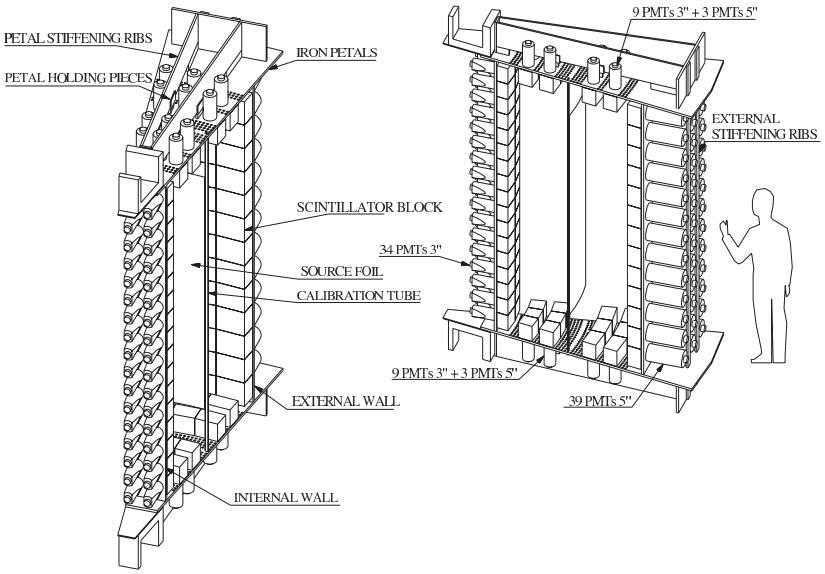

Figure 7 - A schematic view of a single section of the NEMO-3 detector, showing the source strips, calorimeters and structure. The Geiger cell tracking units are not shown.

The scintillator blocks are constructed from low radioactivity polystyrene. The scintillators are cut into seven different shapes in order to cover the entire volume of the tracker and source foils. The thickness of the scintillators is approximately 100 mm throughout, but the width and height ranges between 110 mm and 150 mm. The detection efficiency of the scintillators is 50% at an electron energy of 0.5 MeV. Polymethyl methacrylate (PMMA) light guides are used to transmit light from the scintillator blocks to the PMTs.

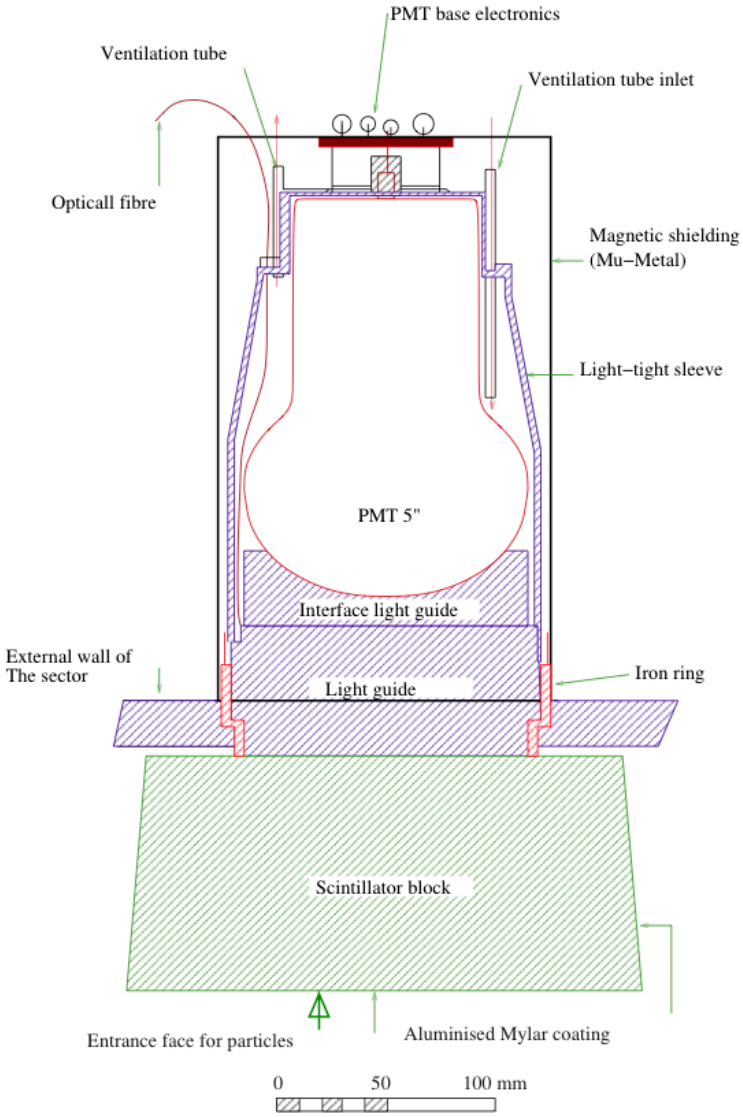

Figure 8 - A schematic view of a single scintillator block attached to a 5" PMT via the use of a light guide. Included is the optical fibre used to calibrate the PMT.

PMTs surrounding the detector convert detected photons into an electrical signal. The number of detected photons is proportional to the energy deposited in the scintillator. The gain of the PMTs is calibrated such that they are able to detect a range of energies up to 12 MeV.[14] A schematic view of a single scintillator block is shown in Figure 8.

The top, bottom and the internal walls of the experiment are covered by 3" PMTs, while the external walls are covered by 5" PMTs. All the PMTs of NEMO-3 were specially produced to have one-third of the radioactive contaminates of a standard PMT. Each of the PMTs is held within black plastic boxes to protect it from external light sources. The

electrical output from a PMT is fed to a discriminator, which returns logic high, when the signal is above a threshold of 48 mV, which is used to trigger the timing circuit.

NEMO-3 has two separate techniques for performing energy calibrations of the PMTs, radioactive source calibration and laser energy calibration.

3.3.1 Radioactive Source Calibration

Periodically, radioactive sources of Bi-207 and Sr-90, of known activities, were placed within the experiment in order to perform energy calibrations. The sources remained within NEMO-3 for approximately 72 hours each time. Bi207 provides two distinct energy spikes of electrons generated by internal conversion; one of 0.482 MeV and the second of 0.976 MeV. The Sr-90 decays to Y-90, which is a pure β emitter with an endpoint energy of 2.283 MeV. This allows the detector to be calibrated for energies up to 3 MeV. These calibrations were not performed with a high frequency as not only did they take 72 hours to perform, but also the PMTs would need to stabilise again before reliable data taking could resume.[16]

3.3.2 Laser Energy Calibration (LEC)

The second method is a relative calibration performed daily by subjecting the PMTs to a flash of light of a known energy. The light is provided by a laser carried by a fibre optic wire directly to the PMT via the interface light guide.

The correction values are then determined as a function of time from when the radioactive source calibration has been conducted and a quality factor is obtained using fit information. The quality is denoted by the LEC flag.

- +1 for bad fit to laser ADC distribution
- +2 for bad linear fit of time dependant corrections
- +4 for maximum correction value > 4 % during the survey period
- +8 for amplitude of correction value > 5 %[17]

3.3.3 Laser Time Correction (LTC)

(3.4)

As the PMTs also trigger the timing measurement for a given event, it is vital the timing calibration be as accurate as possible. The laser system is also used for the time calibration. An LTC value is obtained using the equation

$$C_{LTC}(i,j) = tdc(i,j) - tdc(i,1404),$$

where C_{LTC} represents the laser time correction value, i represents the PMT within the detector and j represents the run number. Run 1404 is chosen as the reference run due to its high stability.[18]

3.4 Radon Trapping

During the first phase of operation, it was discovered that the radon levels within NEMO-3 were approximately 0.7 Bq, which is much higher than the desired background level. In order to reduce the amount of radon gas within the detector, an anti-radon facility was installed in September 2004, which marked the end of Phase-1 and the beginning of Phase-2.

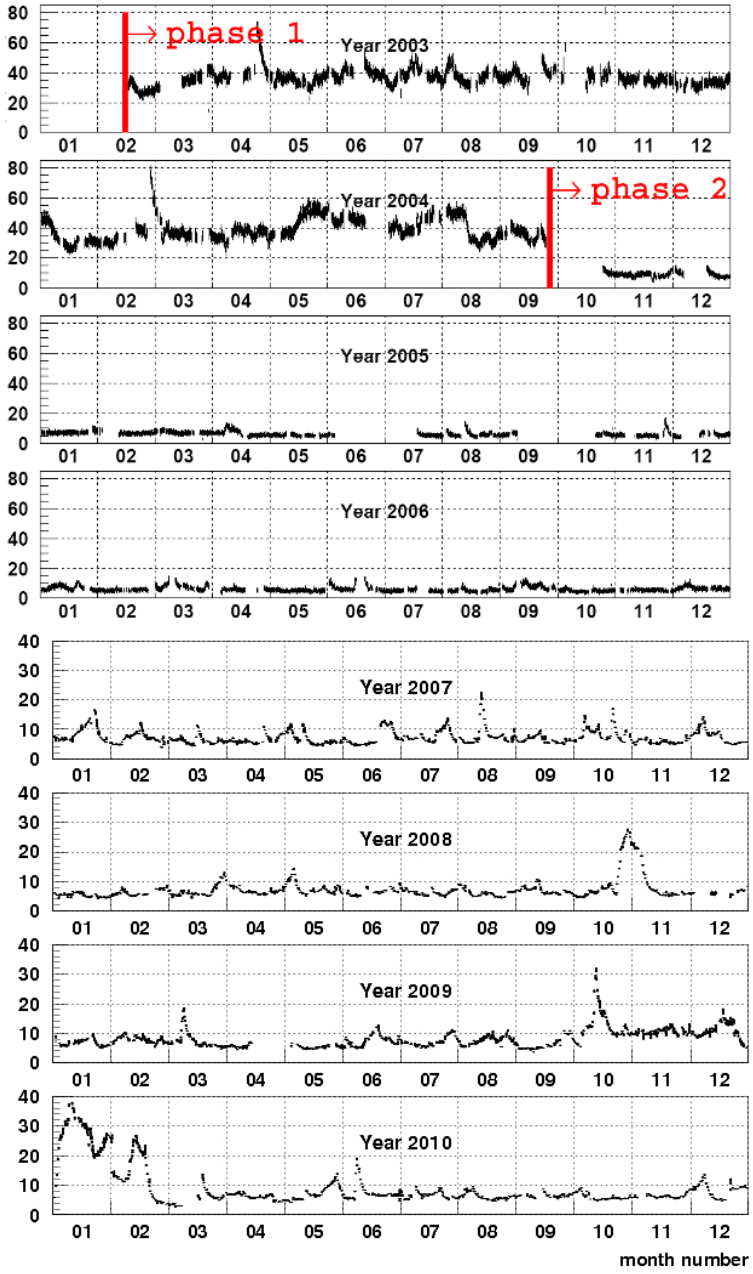

Figure 9 - The activity of radon within the NEMO-3 detector throughout the running period. Months September and October 2004 illustrate the effect caused by the installation of the anti-radon facility.

The anti-radon facility consists of an airtight tent and a radon trap. The airtight tent encompasses the entire NEMO-3 detector within two layers of polyethylene, thus all of the gas entering the experiment had to pass through the radon trapping facility. To trap the radon, the system uses activated charcoal. The charcoal is oxygen treated to create pores in which the radon becomes trapped. Once trapped the radon is held within the

pores longer than the decay time of radon meaning that the gas has decayed before passing into the experiment.

In October 2004, the experiment began collecting data again with the new anti-radon system installed. The new system was measured to reduce the quantity of radon within the detector by approximately a factor of 6.[19] This can be seen in the time-dependent measurement of the radon activity, shown in Figure 9, which depicts the decrease in radon activity between September and October 2004

Chapter 4: Software, Data and Monte Carlo

4.1 Data Collection

The running of NEMO-3 is split into two distinct phases, before the anti-radon facility and after the anti-radon facility, Phase-1 and Phase-2 respectively. Data collection is separated into runs of several hours, which are separated by calibration runs. These Run numbers are used to distinguish between the two phases of data collection. The corresponding start and end dates are given in Table 2.

Phase	Range			
	Start		End	
	Date	Run Number	Date	Run Number
One	15th Feb 2003	1869	21st Sep 2004	3392
Two	4th Oct 2004	3399	1st Jul 2010	8792

Table 2 - The run number and date distribution for the two Phases-1 and 2.

4.1.1 Run Status

Due to a large number of possible causes, a proportion of the runs cannot be trusted to provide accurate data. In order to categorise the potential causes of interference to the

integrity of the data, each run is assigned a run status, which denotes the risk involved. *(see Appendix A)*[20]

4.2 Monte Carlo Generation

Monte Carlo (MC) simulations of the various backgrounds and signals are generated using DECAY0 and GENBB. After being generated the MC is run through a digitiser called NEMOS (based on GEANT-3.21) to introduce effects of the NEMO-3 detector e.g. energy resolution.[21]

4.3 Data Reconstruction

The data collected by NEMO-3 is reconstructed using software called NEMOR. The ultimate purpose of the reconstruction software is to generate 'tracks' for charged particles recorded within the data, but several other processes also occur in order to allow this to be done efficiently.

During reconstruction, it is important to check the status of the Geiger cells used for each track as they may have been switched off or providing extra noise, which could introduce an additional systemic uncertainty to that run. In addition to taking account of the Geiger cell status, NEMOR also applies the laser energy and time correction information where available.

The MC events are also reconstructed using NEMOR but are not subject to the alterations involving laser energy calibration, laser time calibration or Geiger cell information, as these issues are not simulated.

4.4 Event Topology Selection

After the reconstruction process the data and MC is run through the slimming program Slim2 that selects all correctly reconstructed events of a given topology. An electron is selected by the criteria of a negatively charged particle using the track information, with

an associated PMT hit. The same is true for a positron, although a positively charged particle is required instead.

An α particle is determined by two key characteristics:

- its short track length (~200 mm) and therefore no PMT hit,
- delayed detection within the Geiger cells.

The main source of α particles within NEMO-3 is caused by Bi-214 decay, which undergoes a β-α cascade mechanism dubbed BiPo whereby the bismuth-214 decays to polonium-214 via the emission of a β particle. polonium-214 has a half-life of 164 μs before decaying by α emission to lead-210.[23] Therefore, NEMO-3 electronics are able to identify all particles within 700 μs of the first detection as part of the same event. As it takes photons and electrons of the order of nanoseconds to travel through the detector and strike the scintillator walls, it is possible to identify α particles by their delayed emission from this process. The different event topologies and the Slim2 selection requirements are listed in Table 3.

Finally a γ is identified by a PMT as a hit that has no track associated with it. All PMT hits involved must measure an energy greater or equal to 0.2 MeV after energy calibration has been taken into account to remove noise.

Topology Code	Contents of Topology	Slim2 Selection
1e	One electron	Only one negative track associated with one PMT hit.
1e1α	One electron + one α	Only one negative track associated with one PMT hit, with an additional collection of delayed GG cell hits.
1e1γ	One electron + one γ	One track associated with one PMT hit with an addition unassociated PMT hit.
1e2γ	One electron + two γ	One negative track associated with one PMT hit with two additional unassociated PMT hits.
1e3γ	One electron + three γ	One negative track associated with one PMT hit with two additional unassociated PMT hits.
2e & OCE	Two electrons	Two tracks associated with two PMT hits.
2e1γ	Two electrons + one γ	Two tracks associated with two PMT hits and one additional unassociated PMT hit.

Table 3 - The Slim2 requirements for each of the topologies listed, including the desired particle selection.

4.5 The Analysis Package

The final piece of software used is called Ana, which performs the key parts of analysis including:

- Selection – in order to best select as much signal and as little background as possible.
- Plotting – entering the properties of each selected events into Root histograms.
- Scaling – using predetermined activities for the various radioactive backgrounds and run durations to scale the MC histograms.
- Fitting – determining unknown activities by fitting MC histograms to the predetermined MC and data.

(5.1)

Chapter 5: Technique

In order to analyse the data collected by NEMO-3, it is essential to use many pre-existing techniques to reduce the background and isolate the signal. After performing a topology selection, the data and MC is put through Ana, which is used to select the data in order to obtain the best sensitivity to the potential signal. NEMO-3 has several key characteristics, which must be used in the selection in order to extract the signal.

5.1 Internal and External Probability

5.1.1 Theory

The NEMO-3 detector's small diameter does not allow using the time-of-flight (TOF) of a particle directly. Therefore, in order to best discriminate between events originating from the source foil, and from outside the detector, the χ^2 value is calculated and from this a probability of each hypothesis is determined, and then used as selection criterion.

For each hypothesis, internal and external, χ^2 is calculated using the equation

$$\chi^2_{th} = \frac{(\Delta t_{mes} - \Delta t_{th})^2}{\sigma^2_{mes} + \sigma^2_{th}},$$

(5.5)
(5.4)
(5.2)
(5.3)

where Δt_{mes} represents the time difference of the two measured PMT hits, Δt_{th} represents the predicted time difference between the two PMT hits for the given hypothesis, and σ_{mes} and σ_{th} represent the uncertainty of the measure and predicted time differences, respectively. The predicted time differences for each of the hypotheses is predicted using the equations

$$\Delta t_{th}^{\text{int}} = \frac{l_1}{\beta_1} - \frac{l_2}{\beta_2}$$

$$\Delta t_{th}^{ext} = \frac{l_1}{\beta_1} + \frac{l_2}{\beta_2},$$

where l_i represents the particle track length and β_i represents the relativistic factor, which is calculated using the equation

$$\beta_i = \frac{\sqrt{E_i(E_i + 2m_e)}}{E_i + m_e},$$

where E_i represents the energy measured and m_e is the rest mass of the electron. The uncertainty in the predicted time difference, σ_{th}, is calculated using error propagation

$$\sigma_{th}^2 = \sum_{i=1}^{2}\left(\frac{\frac{l_i}{\beta_i} m_e}{\left(E_i\left(E_i + m_e\right)\left(E_i + 2m_e\right)\right)}\right)^2 \sigma_E^2 + \sum_{i=1}^{2}\left(\frac{1}{\beta_i}\right)^2 \sigma_l^2,$$

where σ_E and σ_l represent the uncertainty in the energy measured and the track length respectively.

5.1.2 Application

When calculating the χ^2 probabilities for the internal and external hypotheses using NEMO-3 data, the standard distribution has the majority of the data distributed at low probabilities. The distribution for internal data and external data are shown in Figure 10.

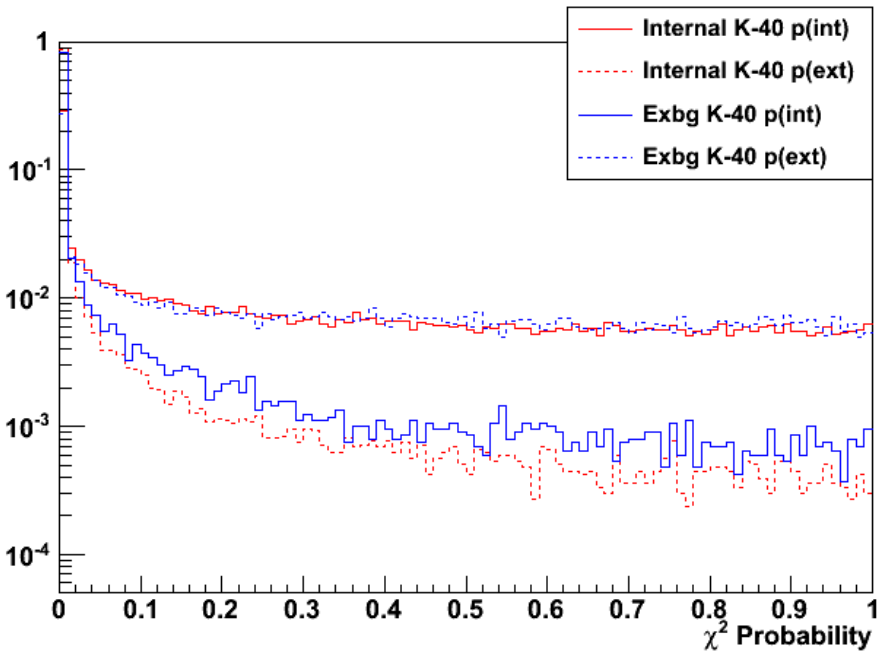

Figure 10 – The χ^2 probability for the internal and external hypothesis calculated for generated K-40 samples using the 2e topology. All samples are shown normalised to 1.

From these distributions the NEMO-3 standard selection criteria are defined as:

- For selecting internal events
    - Internal probability > 4%
    - External probability < 1%
- For selecting external events
    - Internal probability < 1%
    - External probability > 4%

These criteria will be referred to as TOF internal selection and TOF external selection in the rest of this thesis.[24]

5.2 Laser Energy Correction

Depending on the quality of the laser energy correction process, flags are assigned to each PMT for each run. These flags are then used to determine whether the event is a viable candidate for inclusion within the datasets. Earlier studies performed using NEMO-3 data showed the optimum value is to remove all events with a LEC flag > 2, using the flags described in Section 3.3.2.[25] It is also found that when there is no LEC correction value available, it is important to reject these events, as the energy is not corrected during reconstruction.

5.3. Foil Boundaries

In order to best define the geometric boundaries of the Nd-150 foil, a study was performed by NEMO-3. The expected physical dimensions are not found to be optimum for removing background events introduced by neighbouring foils. Therefore the geometric fiducial region is defined as:

- $-117 < Z < 117$ cm
- $1.802 < \Phi < 1.847$ rad. [25]

The geometric distribution of 2e events can be seen in Figures 11 and 12.

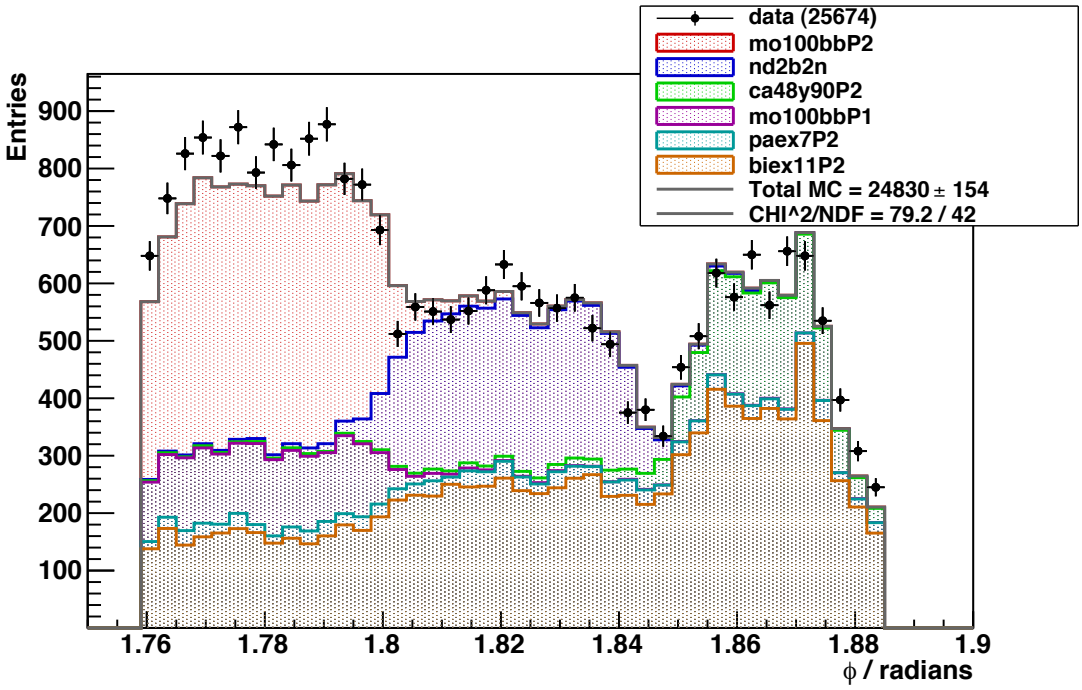

Figure 11 - The event vertices of 2e events with distributed in ϕ. It is possible to discern the boundaries between source strips. (see Appendix D for legend key)

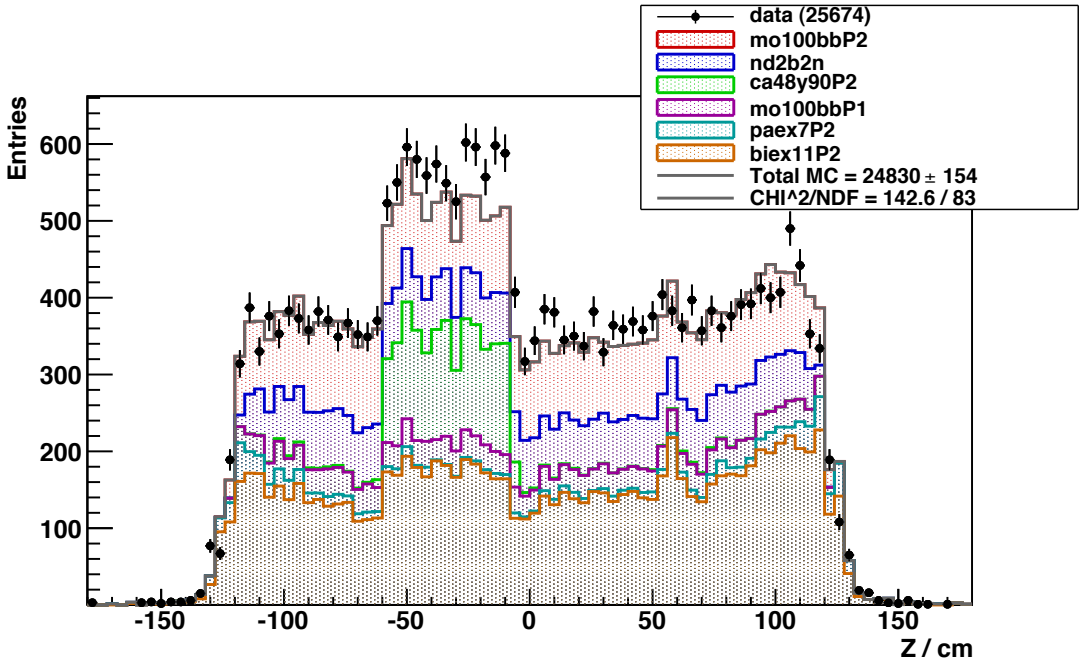

Figure 12 - The event vertices of 2e events, distributed in the Z coordinate.

(see Appendix D for legend key)

Chapter 6: Backgrounds

Due to NEMO-3 being a low radiation experiment, it is vital to the analysis of double β decay to understand all of the sources of background radiation within the detector; particularly those that are able to mimic double β decay. For this reason, it is necessary to construct a background model consisting of the isotope, location and activity of each contaminant. The complete background model is subdivided into three parts:

- the internal model, made up of all the homogenous contaminants within the source foils
- the external model; all background that is not within the foil
    - Phase-1
    - Phase-2
- the heterogeneous background contaminations (i.e. hotspots).

6.1 External Background Model

A survey of the entire NEMO-3 detector, conducted in 2009 using the data collected up until that point, determined the global external background model for the detector in both Phases-1 and 2. *(see Appendix B)* Although this global model includes the Nd-150 foil, it is important to check its validity in the local region. Especially as there is a note

within the study that stated that Sector 5 appears to contain less background contaminants than the other 19 sectors. [27]

In order to validate the model, three topologies are used, OCE (One Crossing Electron), 1e1α and 1e1γ. Both OCE and 1e1γ are used in conjunction with the external TOF selection, but this criterion cannot be applied to the 1e1α topology, which is used to access internal and external backgrounds simultaneously. The topology 1e1α only contains a single PMT hit and therefore a TOF cannot be obtained for calculating an internal or external hypothesis.

OCE requires the event to consist of two oppositely curved tracks, both associated with a PMT hit. This topology describes an electron that has been emitted from decay outside the foil, which has then passed through the foil, and hit the scintillator wall on the other side.

The 1e1γ topology does not require a specific curvature (charge) on the track of the electron/positron to allow for both types of particle and for both directions of flight to improve statistics.

6.2 1e1α Analysis

The analysis software, Ana, is not equipped to select the 1e1α topology and thus there has been minimal examination of this topology within previous analyses. As reconstructed data from NEMOR does not contain information on α particles, i.e. they are not reconstructed; an algorithm has been developed to cluster Geiger cells into candidate α particles.

6.2.1 Clustering Algorithm

In order to create an α object the program loops over all delayed Geiger cell hits checking whether they are within:

- 15 cm in radius
- 15 cm in ϕ
- 20 cm in Z

of another delayed Geiger cell hit. If all three of these spatial criteria are true, then the two cells are 'linked' and stored in an array. Once every possible permutation of delayed Geiger cells has been tested, the array of linked Geiger cells is looped over by checking all items against all previous items in the array using a second loop. If a cell is found to be common to two different linked pairs, the three Geiger cells are joined together in a cluster. Pairs that return 'true' are subsequently added to this cluster until the second loop is finished. Then the process begins with the next linked pair in the array, creating a new cluster object.

Finally all clusters are checked for common Geiger cells with another cluster. If this is found, the larger cluster must contain all of the cells of the smaller cluster by definition, therefore the smaller cluster is deleted. This leaves an array of completely separate and unique clusters.

6.2.2 Delay/Decay Time

In order to confirm the effectiveness of the clustering algorithm and the selection process of selecting the BiPo mechanism, a plot of the mean delay time between the detection of the electron and the clustered Geiger hits is shown in Figure 13. The data is expected to describe the decay time of Po-214, which has a half-life of 164 μs.

Using the selection criteria:

- Event vertices must fall within the Nd-150 foil
- Each event must contain 4 clustered delayed hits
- The mean delay time for the delayed hits > 90 μs,

the distribution in Figure 13 is created using both Phase-1 and 2 data. The fit shown in Figure 13 yields a half-life of 178±11 μs, which is agreement with the established half-life of 164 μs.[23]

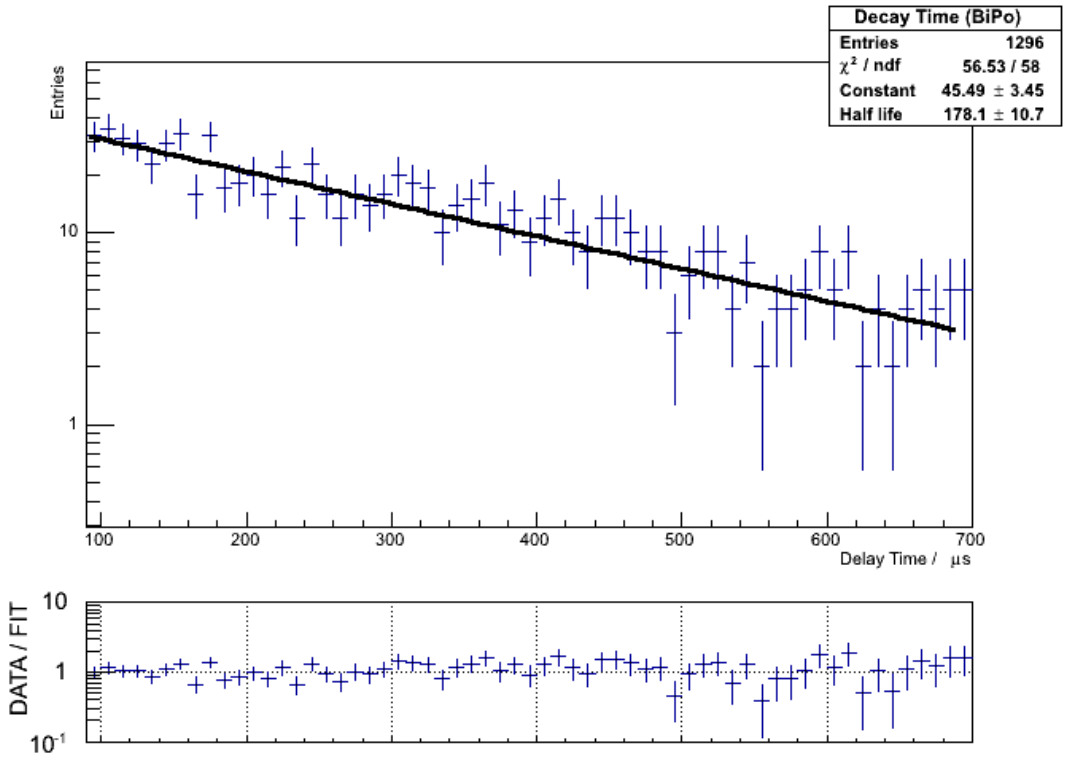

Figure 13 – Distribution of the delay between the emission of a β particle and the following α particle in the BiPo mechanism. The plot includes a fit returning a half-life of 178±11 μs.

6.2.3 Bi-214 Backgrounds

Data from Phase-1 and Phase-2 is processed separately, but using identical selection criteria, therefore it is possible to compare the relative activity change between the phases without requiring an efficiency of the selection process, given in Table 4.

Phase	No. of Events	Total Time of Selection (s)	Events/Time (s^{-1})
One	679	29,478,404	23 (±1.3) ×10^{-6}
Two	617	97,409,992	6.3 (±0.4) ×10^{-6}

Table 4 - The number of events selected for each phase of running, including the phase durations and the relative Bi-214 activities, not taking into account efficiency of selection.

The uncertainties are estimated by fitting Phase-1 and Phase-2 individually with the half-life parameter fixed to the world-average value of 164 μs.[23] A linear relationship is found between the number of events and the constants returned from this fitting program, as demonstrated in Figure 13. The error in these constants is propagated to give a statistical error on the number of expected events in the given time frames. A relative decrease in Bi-214 by a factor of 3.7±0.4 is observed for Phase-2, which is approximately half of the global reduction by a factor of ~6 as discussed in section 3.4. This is most likely due to the component of Bi-214 from within the foil itself, which does not change from Phase-1 to Phase-2.

The program Ana is used to test the validity of the global background model for Bi-214 and to estimate a value of Bi-214 lying on the surface of the foil, which was previously unmeasured. For this study, the selection criteria are loosened to include events that display a mean delay of as little as 30 μs instead of 90 μs.

As all samples fitted in this topology are from Bi-214, the typical technique of using the energy spectrum to fit the samples is of no use, instead the samples are fitted using the first Geiger cell layer that the electron struck, as this best provided a geometric distinction between source locations. Shown in Figures 14.a and 14.b is the first layer the electron track stuck, which is used to discriminate between geometric locations of the Bi-214. Figures 14.c-f and Figure 15 are used to evaluate the effectiveness of selecting the BiPo mechanism.

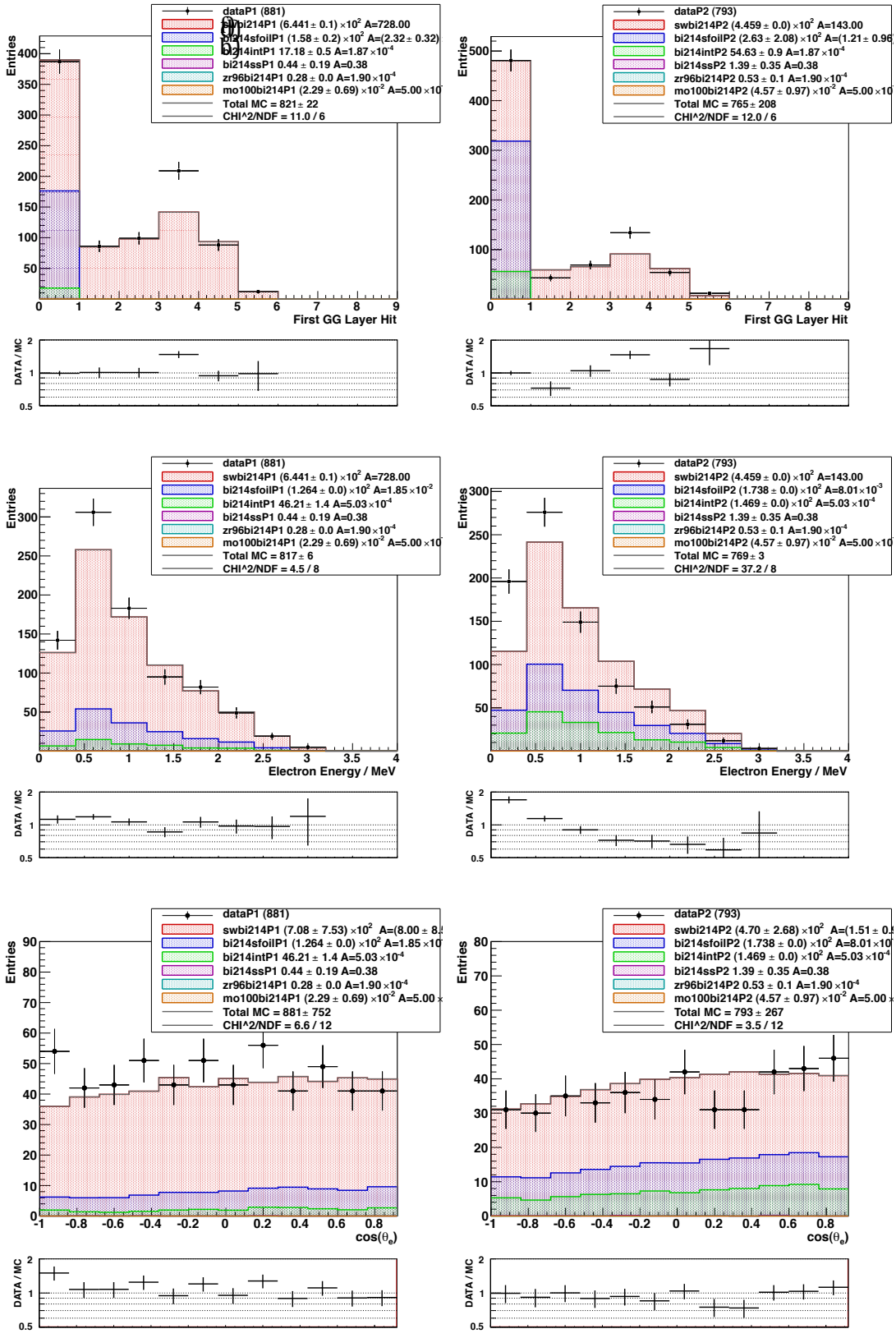

Figure 14 - Using the 1e1α topology, distributions of first Geiger cell struck by the electron, electron energy and cosine of the angle between the electron and the normal of the foil. Plots a), c) and e) are of Phase-1 and plots b), d) and f) are of Phase-2. (see Appendix D for legend key)

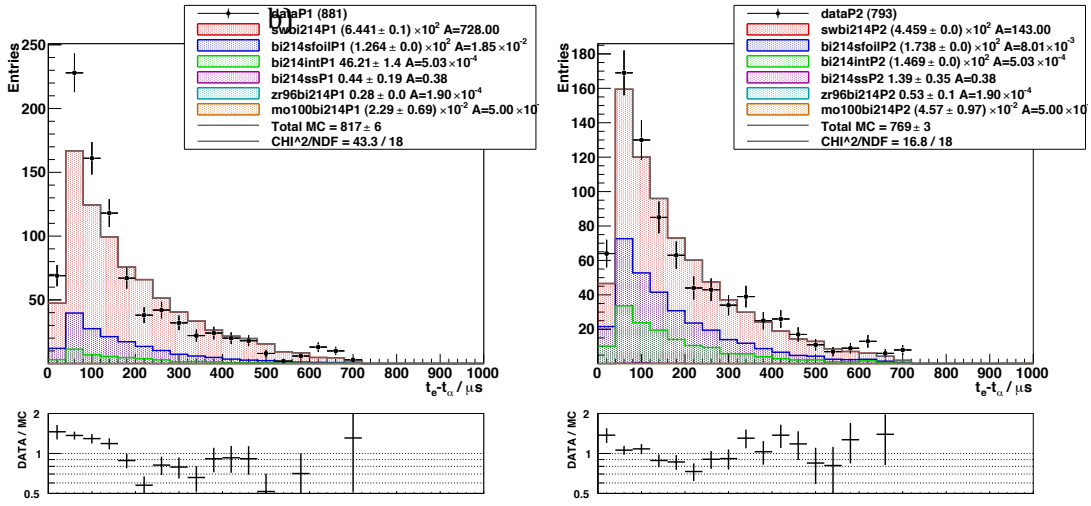

Figure 15 - Using the 1e1α topology, distributions of the delay times are shown. Plot a) is of Phase-1 and plot b) is of Phase-2. (see Appendix D for legend key)

Using Figures 14.a and 14.b the values of Bi-214 from the sources of SWIRE (Surface of the Wire) and SFOIL (Surface of the Foil) are fitted and the results are shown in Table 5.

	SFOIL / mBq	SWIRE / mBq
Phase One	18.5	728
Phase Two	8.01	143

Table 5 - The activities of Bi-214 positioned on the surface of the foil (SFOIL) and on the surface of the wires (SWIRE) for each of the phases. (see Appendix D for legend key)

Certain anomalies remain unanswered. The main query is the ill-fitting electron energy distribution, particularly in Phase-2. This will require further work to understand, as all the samples selected by the 1e1α selection were Bi-214 and therefore have the same energy distribution.

A second anomaly is the systematically high data count for the fourth Geiger cell layer (layer 3). A range of selections was attempted, including increasing the minimum delay time and energy cutting to understand the source of this phenomenon, but no result was found. It is possible that there is a source of Bi-214 that is currently un-simulated.

6.3 1e1γ Analysis b)

The 1e1γ topology is used to assess the external background around the Nd-150 foil. The following other selection criteria are used:

- -120 < Z < 120 cm, 1.802 < Φ < 1.882 radians
- External TOF hypothesis *(see Section 5.1.2)*
- Good Run Status *(see Section 4.1.1)*
- Good PMT Status
- LEC Selection. *(see Section 5.2)*

These events can originate from a range of locations including the air under the iron shield (EXBG-2), the iron shield itself (EXBG-4), the PMT shield (EXBG-8) and the PMT glass (EXBG-11).

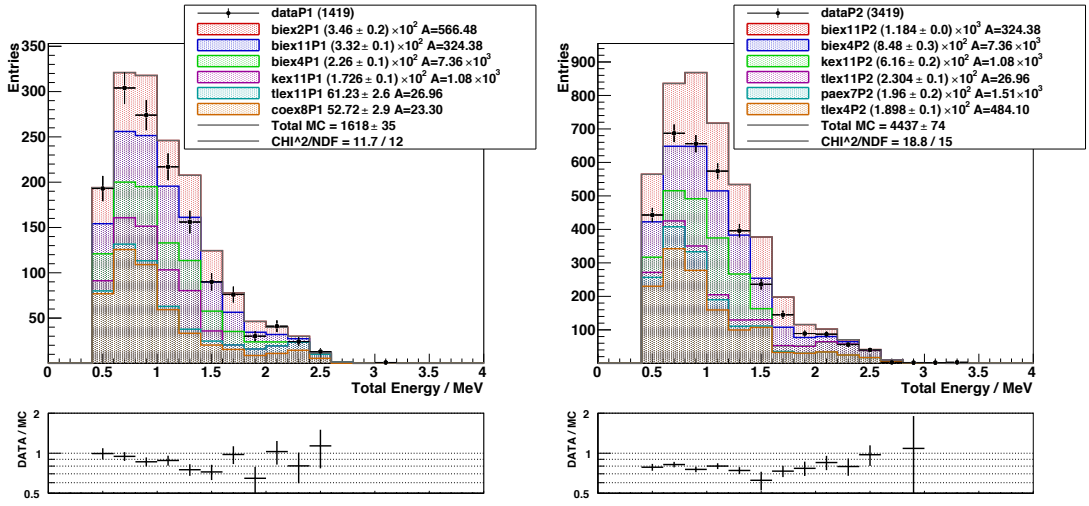

Figure 16 - The 1e1g topology total energy distributions. Plot a) is of Phase-1 and b) is of Phase-2. (see Appendix D for legend key)

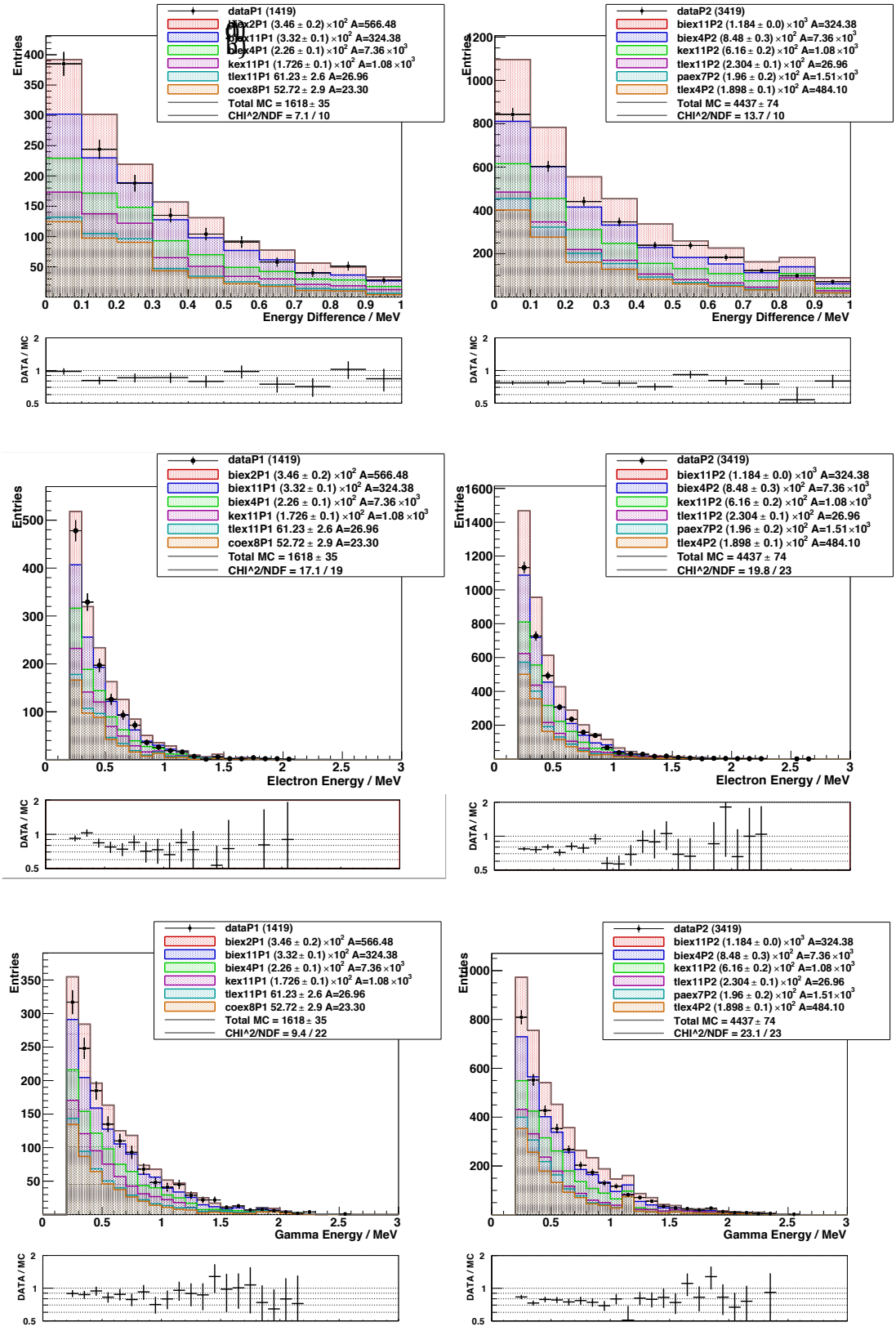

Figure 17 - The 1e1g topology energy difference, electron energy and gamma energy distributions. Plots a), c) and e) are of Phase-1 and b), d) and f) are of Phase-2. (see Appendix D for legend key)

The 1e1γ topology has few events and thus a larger statistical uncertainty but remains a useful probe in determining the external background model. The data in the 1e1γ topology does not show good agreement with the global external background model within the geometric region of interest. An over-estimation of the MC is shown in Figures 16.a-b and Figures 17a-f, as predicted for Sector 5. This overestimation begins at 14±3% for Phase-1 and rises to 30±2% for Phase-2. As all isotopes appear to be causing the overestimation, opposed to a single source, it is hypothesised this may be caused by the NEMO-3 detector being less efficient in the region of Sector 5.[26] For this reason the background model using these distributions is not altered. Further work is being conducted by the NEMO collaboration to determine the source of this deviation of the MC and data.

6.4 One Crossing Electron (OCE) Analysis

As all events reconstructed by NEMOR under the assumption that the event has originated from the foil, every electron track has the polarity of the charge determined by the sign of curvature. Therefore, electrons travelling from the face of the scintillator towards the foil will obtain a positive charge. Using this information, events are selected if there are two tracks that have scintillator hits associated and opposite charge designation.

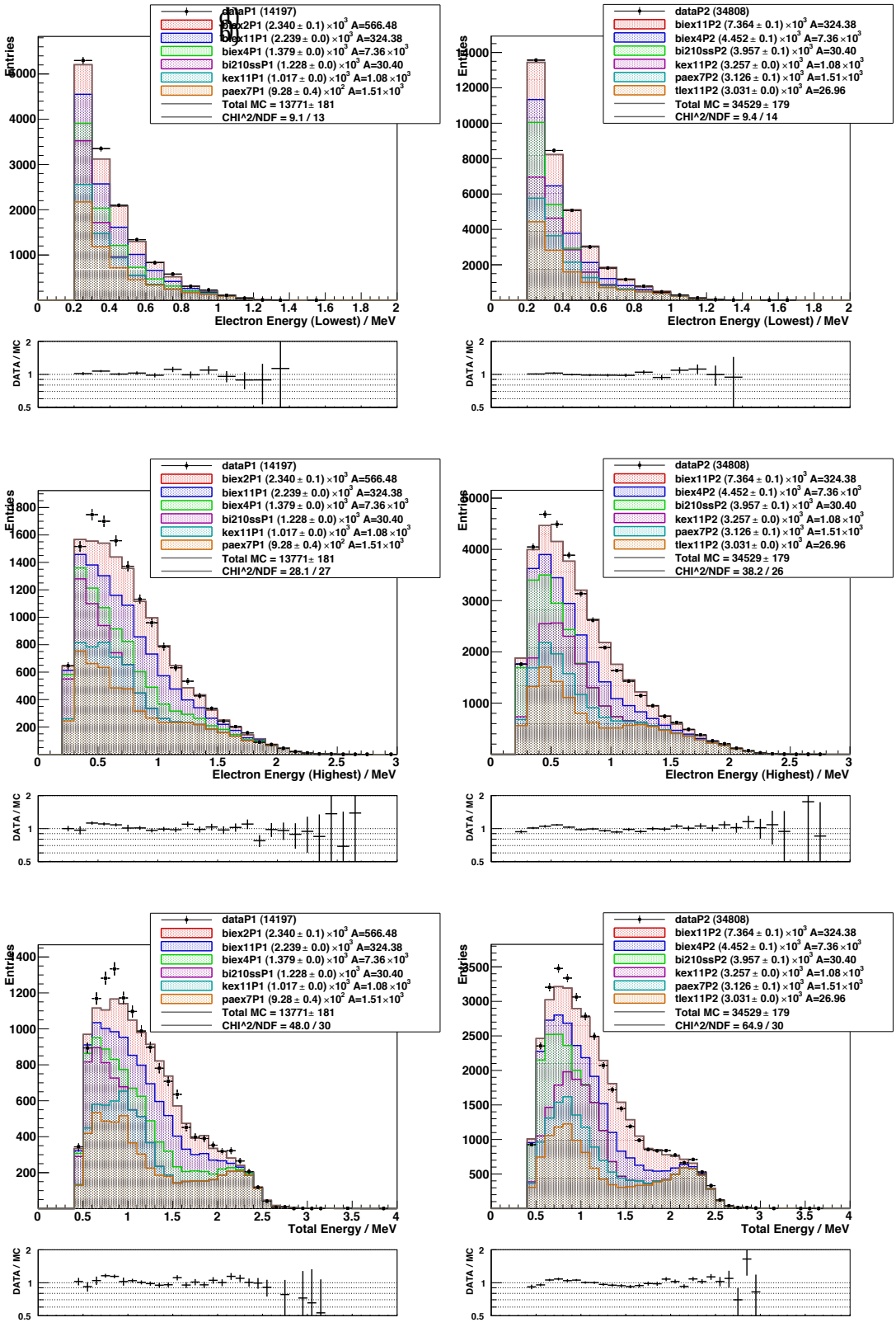

Figure 18 - The OCE topology distributions of least and most energetic electrons and total energy. a), c) and e) are of Phase-1 and b), d) and f) are of Phase-2.
(see Appendix D for legend key)

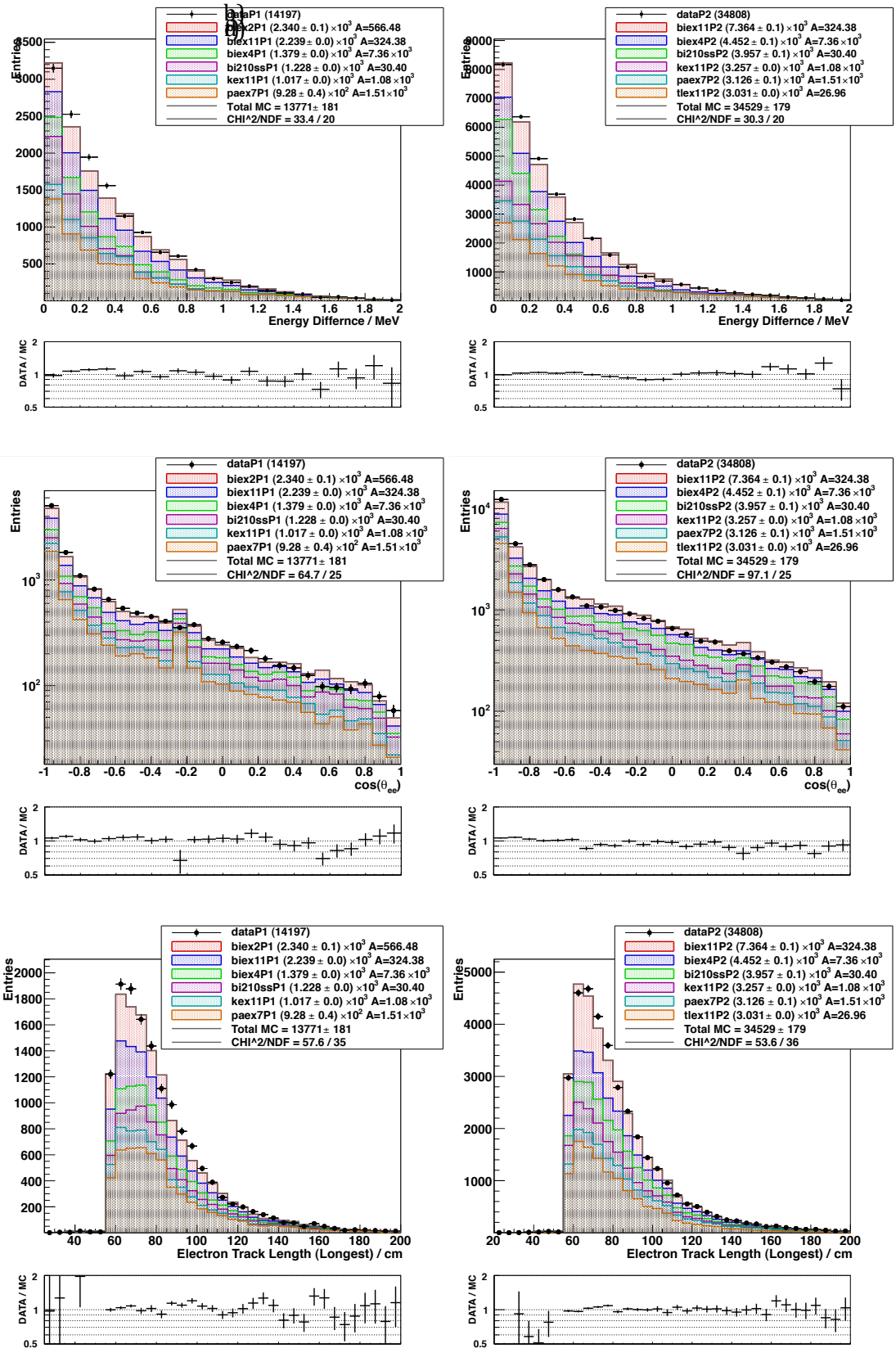

Figure 19 - The OCE topology distributions of energy difference, cosine between tracks and the longer track length. a), c) and e) are of Phase-1 and b), d) and f) are of Phase-2. (see Appendix D for legend key)

The distributions of total energy of the two electrons and of the more energetic electron, shown in Figures 18.c-f, displays a surplus in MC events at low energies. This is not visible within the distribution of the less energetic electron (Figures 18.a and 18.b) and the deviation seen in the two distributions is fully correlated. All other distributions, Figures 19.a-f, show good agreement. Apart from the discrepancy at electron energies below 1 MeV, the external background model is deemed to be of a sufficient quality, in both phases, for all samples in which OCE is sensitive to. Further improvements to the model using the fitting tool are limited by the narrow range of 0.4 to 0.6 MeV and statistics.

6.5 Internal Backgrounds

After defining the external background model for the local region, it is essential to check the validity of the internal background model. Double β decay can be mimicked by a combination of a standard β decay and scattering within the foil or an additional electron emission from internal conversation as depicted in Figure 20.[26]

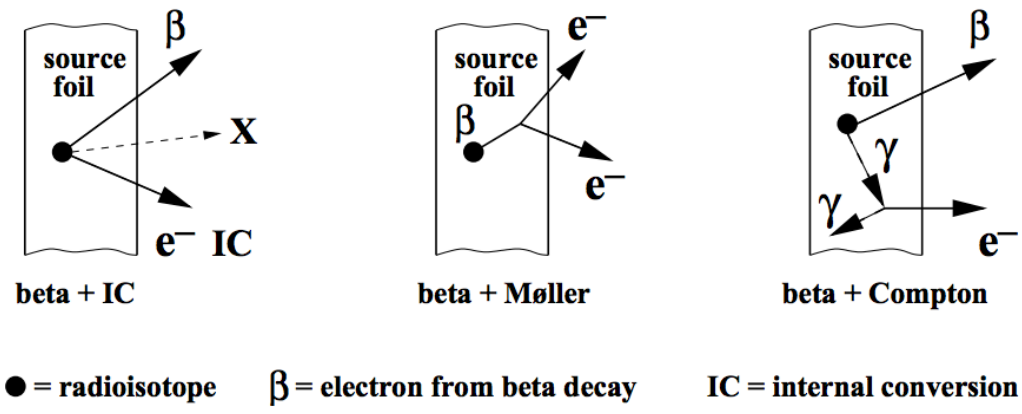

Figure 20 - Three methods in which standard beta decay is able to mimic double beta decay, via the mechanisms of Møller or Compton scattering or internal conversion.

An internal background model for the Nd-150 foil had already been outlined by previous studies, which was incorporated within this analysis.

6.5.1 Hotspots (Heterogeneous Backgrounds)

Before attempting to validate the internal model for the homogenous backgrounds within the Nd-150 foil, it is important to remove the influence of any heterogeneous backgrounds within the foil. In order to best identify localised regions of contaminations (hotspots), the vertex positions of events are plotted for the topologies 1e, 1e1γ, 1e2γ and 2e, shown in Figure 21. Visible in Figure 21 is the structure of the source foils.

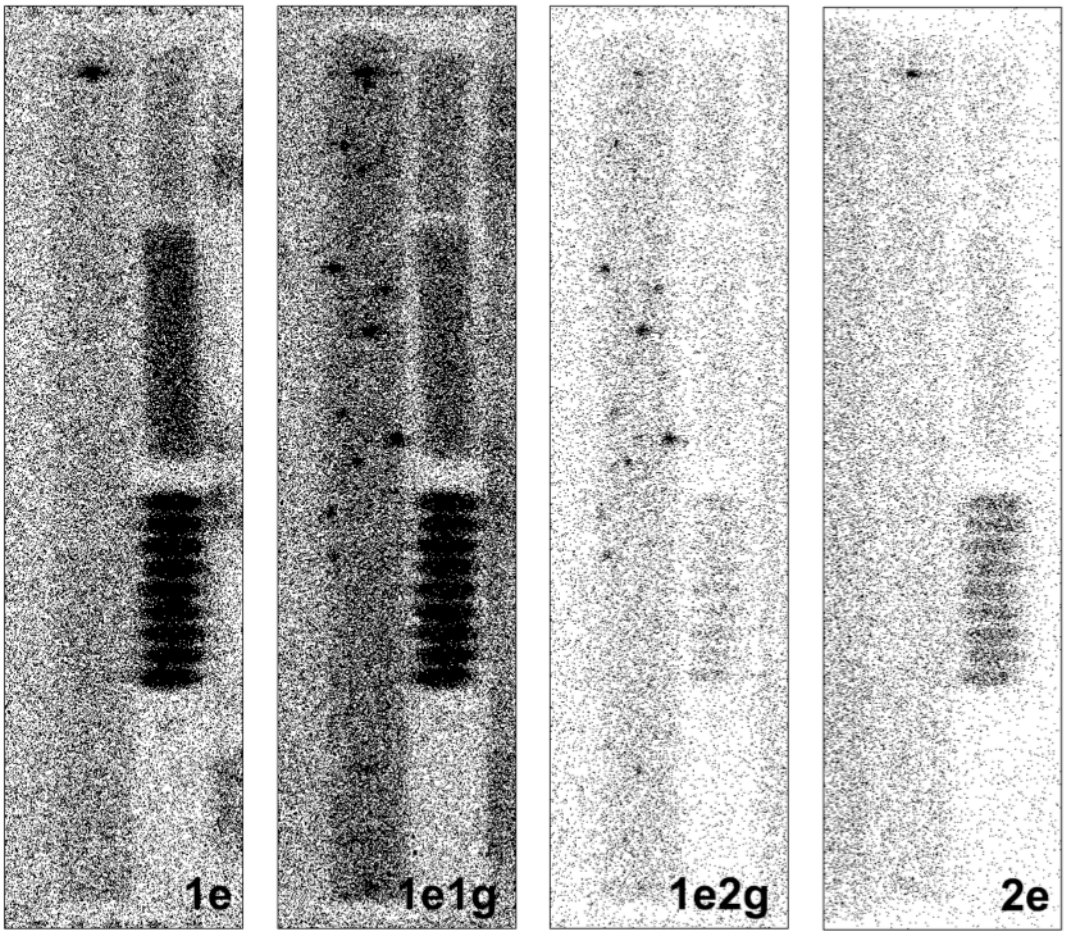

Figure 21 - The vertex positions of four different topologies, 1e, 1e1g, 1e2g and 2e. It is possible to observe the structure of the foils within strip 6 and 7 of sector 5.

6.5.2 Pa234m Hotspot

Within all four topologies is a highly active hotspot located near the top of the foil. From previous studies of the Nd-150 foil, this hotspot is known to be due to Pa-234m.[26] To maximise the number of events in the final sample, the most efficient selection on the

geometric area is used to ensure that the data is neither wasted nor biased. The centre of the hotspot is determined for the two dimensions Z and sector number separately. A double Gaussian fit is used on both dimensions to determine a value of radius in each dimension, shown in Figures 22 and 23.

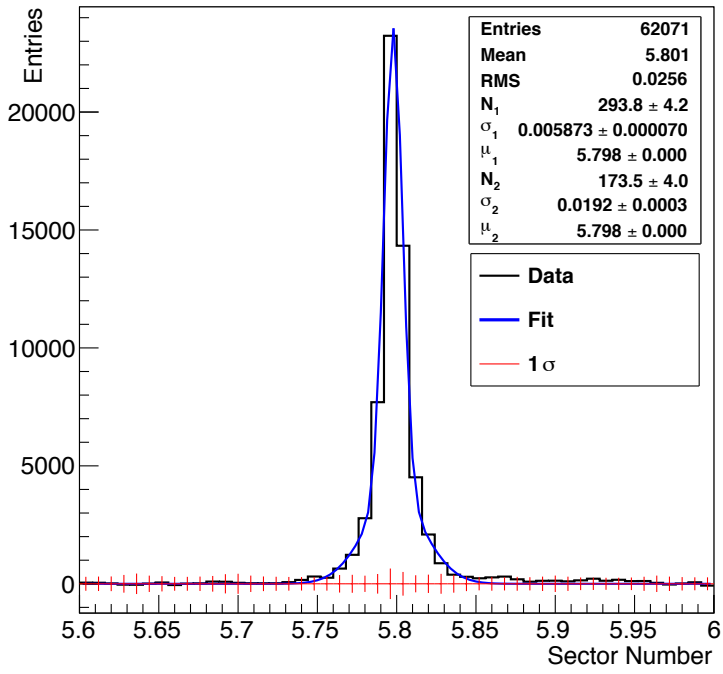

Figure 22 - Phase-1 and 2 a distribution of isolated data events from the Pa-234m hotspot in sector number. The distribution is obtained by subtracting the predicted number of events from the region containing the spike.

(6.1)

(6.2.2)

(6.2.3)

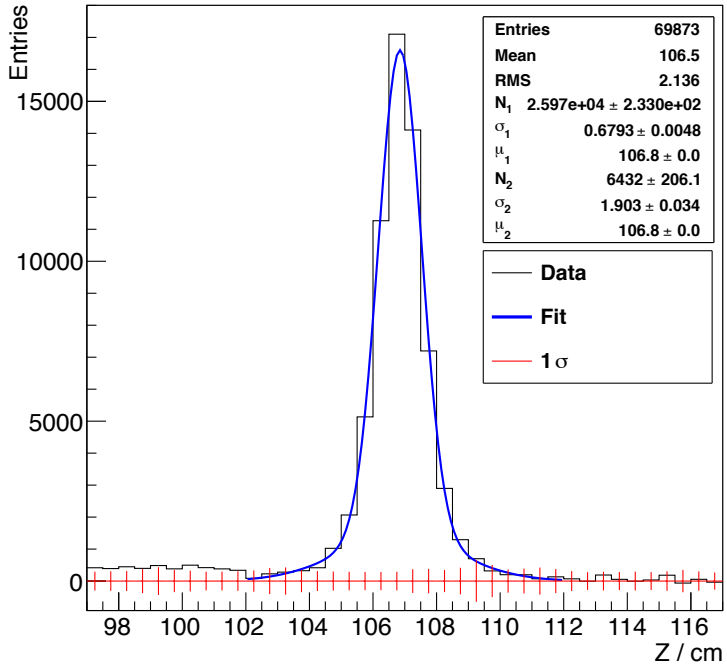

Figure 23 - Phase-1 and 2 a distribution of isolated data events from the Pa-234m hotspot in Z. The distribution is obtained by subtracting the predicted number of events from the region containing the spike.

From these fits, it is determined that the Pa-234m hotspot can be approximated to be circular in shape. Therefore the new selection is defined as,

$$\left(R \times \left(\phi - \phi_{hs}\right)\right)^2 + \left(z - Z_{hs}\right)^2 < r_{hs}^2$$

where R represents the radius of the foil (154.9 cm), ϕ and z represent the position of the event in sector number and the Z-axis respectively and ϕ_{hs}, Z_{hs} and r_{hs} represent the sector number and Z position of the centre of the hotspot, and the radius of the hotspot, which are:

$$\phi_{hs} = 1.821 rad$$
$$Z_{hs} = 106.8 cm$$
$$r_{hs} = 2.5 cm$$

.

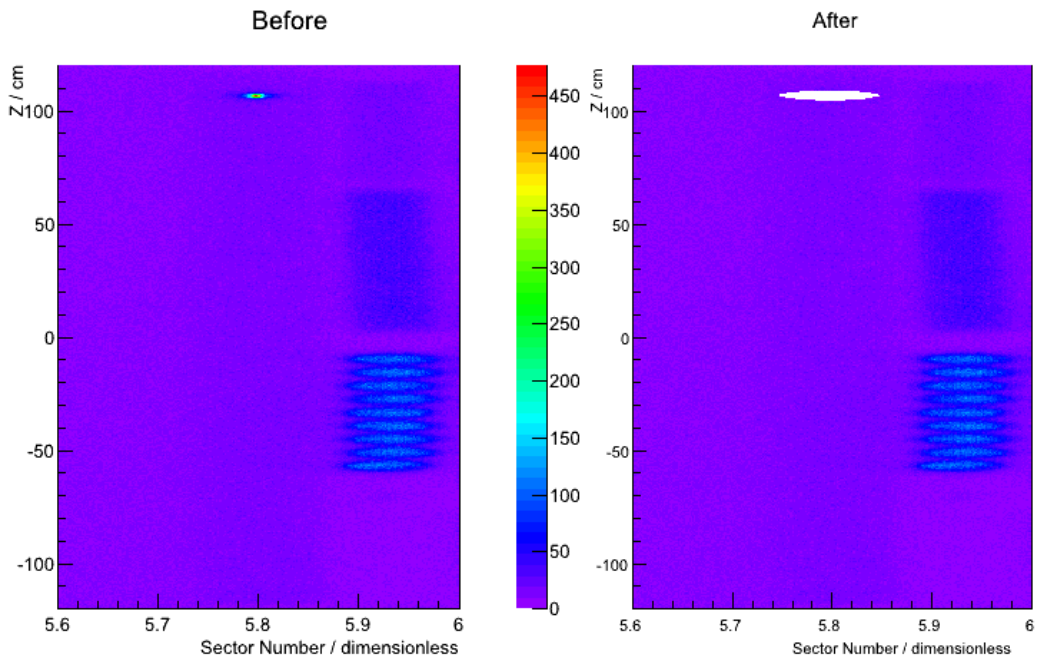

Figure 24 - Two two-dimensional distributions of event vertices in sector number and Z. The left panel shows the distribution before the circular Pa-234m selection and the right shows it after the selection.

From Figure 24, which shows the distribution of 1e event vertices along the foil, it is possible to determine that most bins within the Nd-150 foil have < 50 events in the 1e topology, while the most active bin(s) of the hotpot region surpass 450 events. Using a geometric requirement will decrease the number of signal events in the final sample, as well as the Pa-234m contaminations.

Using the activity determined in the previous study conducted by NEMO-3, it is possible to estimate the loss of signal caused by the geometric requirement. Approximately 1.3% of the geometric area of the Nd-150 foil is lost, which will be taken into account in the final efficiencies of the selection.

6.5.3 Bi-207 Hotspots

Several significant hotspots in the Nd-150 foil are observed within topologies containing a γ emission; therefore it is not necessary to remove these regions from the final half-life

analysis. However it is important to understand, and potentially remove, these from the verification of the internal background model.

Using energy distribution plots, as with the Pa-234m hotspot, it is determined that these hotspots are all due to Bi-207, which can decay via electron capture to Pb-207, which produces either one or two γ in order to stabilise, seen in Figure 25. An electron is also emitted via internal conversion.

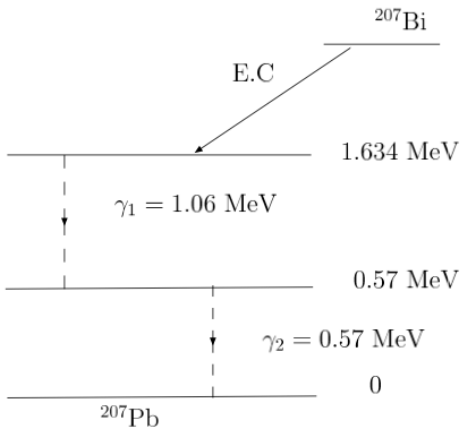

Figure 25 - Excitation diagram of the decay of Bi-207 to Pb-207 via electron capture and the emission of two photons.

In order to best identify the location of all the Bi-207 hotspots, the 1e2γ topology is chosen as being the optimum option between sensitivity to Bi-207 and amount of data collected, as is shown in Table 6.

Channel	Normalised Proportion of Bi-207
1e	0.0448
1e1γ	0.573
1e2γ	1
1e3γ	0.889
2e	0.0513
2e1γ	0.172

Table 6 - The normalised relative proportion of Bi-207 to data in each topology.

The selection criteria for the energy distributions are:

- channel 1e2γ *(see Section 4.4)*

b)

- all particles detected must have > 0.2 MeV

Using these selection criteria the following distributions are generated to demonstrate kinematic patterns within Bi-207 that were used to identify Bi-207 events. The distributions are normalised by weighting to treat the MC and data as though they had the same number of events.

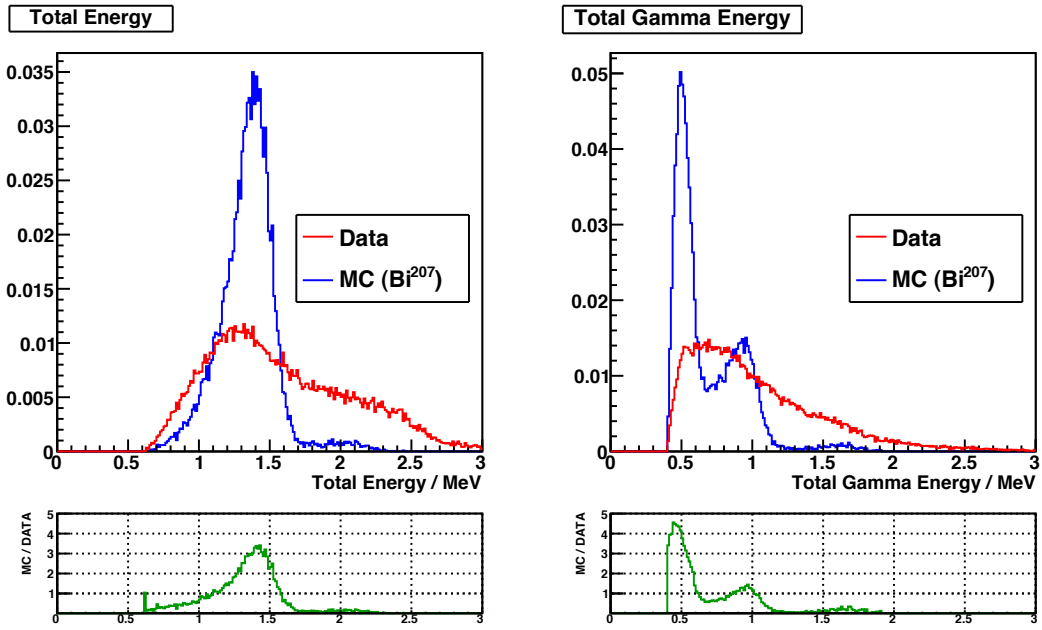

Figure 26 - The distributions of data collected for Phase-1 and 2 are in red, while MC of internal Bi-207 is normalised to the data in blue. Below, in green, highlights the division of MC by data to observe the best regions for selecting in total energy (a) and in total gamma energy (b).

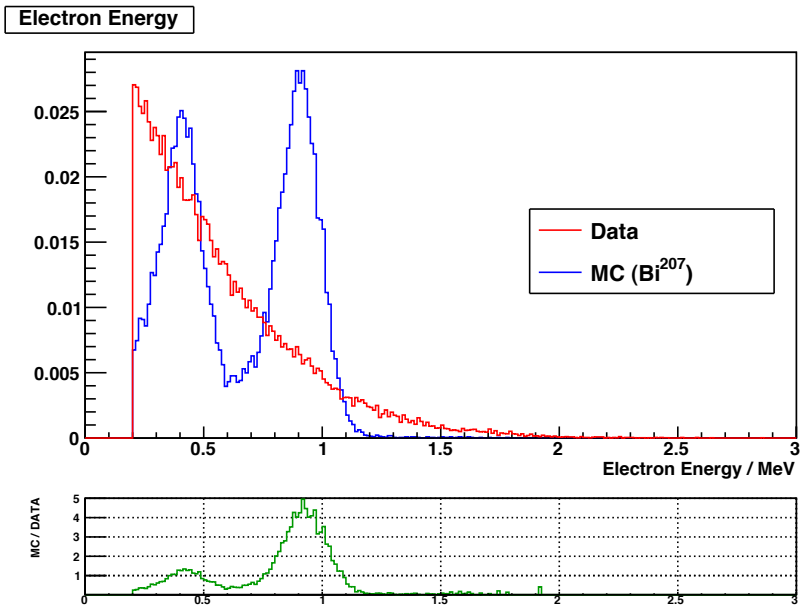

Figure 27 - The distributions of data collected for Phase-1 and 2 are in red, while MC of internal Bi-207 is normalised to the data in blue. Below, in green, highlights the division of MC by data to observe the best regions for selecting in electron energy.

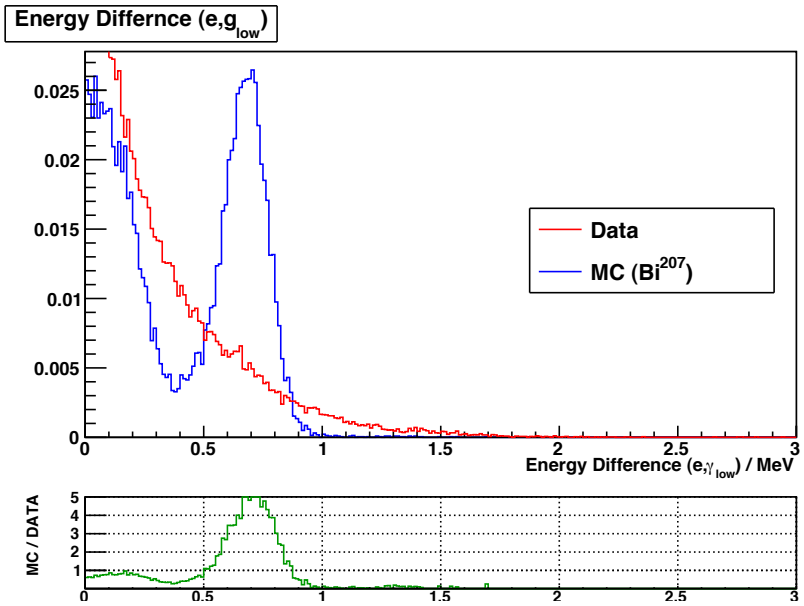

Figure 28 - The distributions of data collected for Phase-1 and 2 are in red, while MC of internal Bi-207 is normalised to the data in blue. Below, in green, highlights the division of MC by data to observe the best regions for selecting in gamma energy.

The kinematic distributions in Figure 26-28 showing regions of concentrated Bi-207 events, displays the largest differentiation between the data set and the simulated Bi-207 signal. From the plots above the following selection criteria are derived:

- 1.1 MeV < Total Energy of the 1e2γ Topology < 1.6 MeV
- Total Gamma Energy < 1 MeV
- 0.35 MeV < E(e) < 1.1 MeV
- 0.5 MeV < |E(e) – E(γ_{high})| < 0.95 MeV

In addition to these criteria, only events in the region -120 cm < Z < 120 cm are used to generate the two-dimensional distributions of event vertices shown in Figure 29.

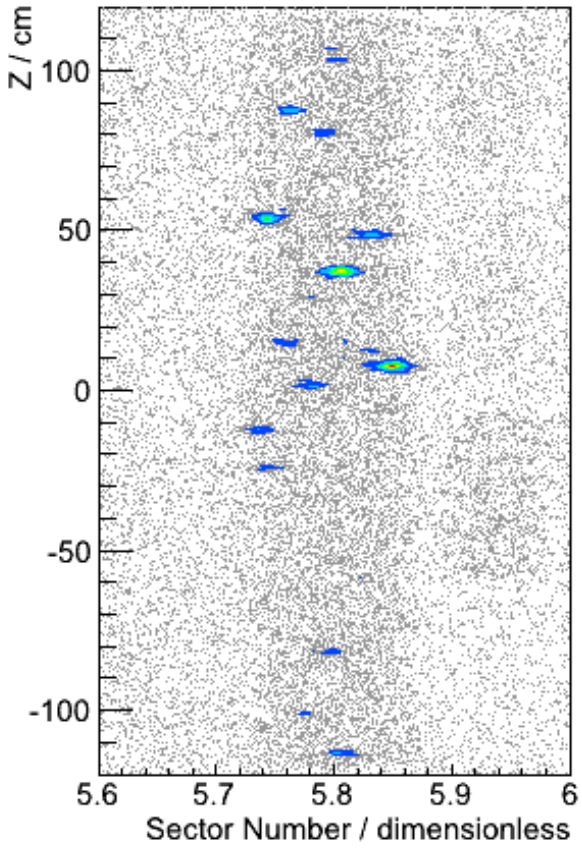

Figure 29 - A two dimensional plot of 1e2γ event vertices distributed in sector number and Z. Grey depicts all event vertices for data. The coloured regions represent the data selected.

The hot-region above 100 cm, shown in Figure 29, is believed to be due to the Pa-234m hotspot already visible in the 1e selection *(see Section 6.5.2)*. The other 15 hotspots shown are considered not to represent a large proportion of the total amount of Bi-207 in the foil and can be represented as part of the homogenous internal background model, due to their non-occurrence within the 2e topology. While using the 1e1γ and 1e2γ topologies to fit the internal background model and for estimating the systematic uncertainties, the three largest hotspots are removed Events are removed events if the vertex of the event falls in any of these areas:

- $1.82 < \phi < 827$ radians and $34 < Z < 42$ cm
- $1.836 < \phi < 1.842$ radians and $6 < Z < 12$ cm
- $1.801 < \phi < 1.809$ radians and $52 < Z < 55.5$ cm

In future studies of the excited decays of Nd-150 it will become important to take these heterogeneous backgrounds into account as the primary analysis topologies include γ.

6.5.4 1e1γ Channel

The most recent version of the external background model, coupled with the pre-existing Mo-100, Nd-150, Zr-96 and Ca48 models, are used for the kinematic distributions of the Phase-1 and 2 data. The selection criteria are:

- Channel 1e1γ *(see Section 4.4)*
- Each particle must have an energy > 0.2 MeV
- All event vertices must fall within
    - -117 cm < Z < 117 cm
    - 5.7374 < sector number < 5.8735
- TOF internal selection *(see Section 5.1.2)*

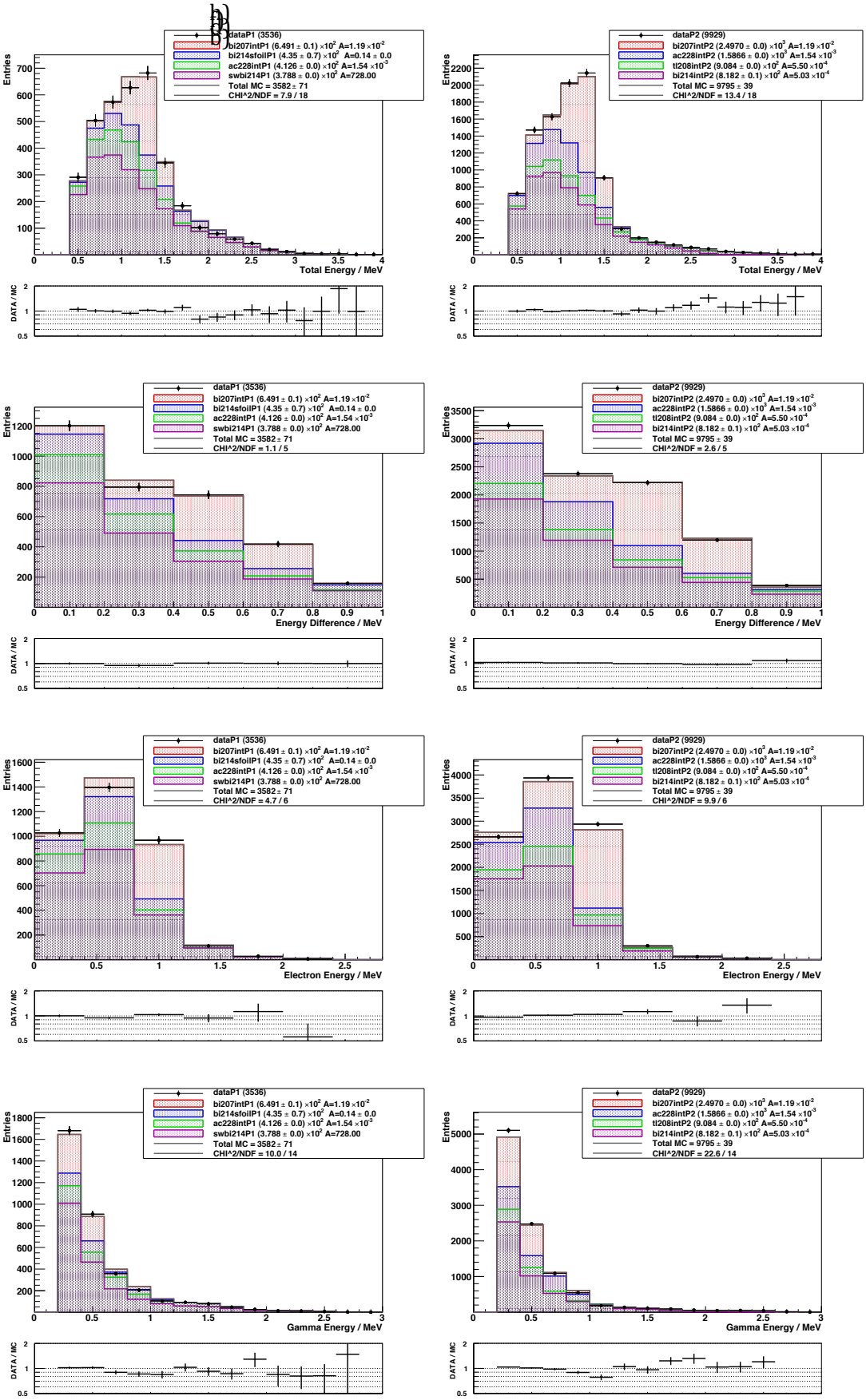

Figure 30 - Distributions of total energy, energy difference, electron energy and photon energy of the 1e1γ topology. a), c), e) and g) are of Phase-1 and b), d), f) and h) are of Phase-2. (see Appendix D for legend key)

b)

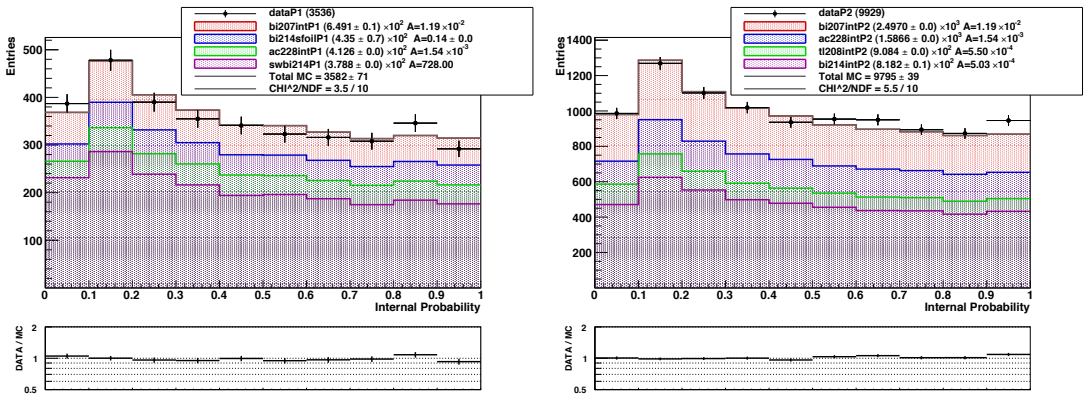

Figure 31 – The 1e1γ topology distribution of internal probability. a) is of Phase-1 and b) is of Phase-2. (see Appendix D for legend key)

The 1e1γ topology is a useful probe in determining the activity of Bi-207 in particular due to the well-defined energy spike shown in the total energy distribution, Figure 31.a and Figure 31.b, and the electron energy distributions shown in Figure 28.e and 28.f.

Using this topology the activities of Ac-228, Eu-152 and Eu-154 are also determined using the entire range of distributions (Figure 31.a-j).

6.5.5 1e2γ Channel

Using the high-energy regions of the 1e2γ topology, it is possible to obtain an area of near pure Tl-208 signal. In order to select internal 1e2γ events, it is necessary to calculate the χ^2 probability of the internal and external hypothesis of each pair (i.e. $e\gamma_1$, $e\gamma_2$ and $\gamma_1\gamma_2$). However, upon examination of these distributions, the internal hypothesis for $\gamma_1\gamma_2$ is found not to correlate with the typical response. The internal hypothesis calculation assumes both particles are emitted simultaneously and this may not be the case for $\gamma_1\gamma_2$, therefore this parameter is not used in the selection. However the external hypothesis is still used.

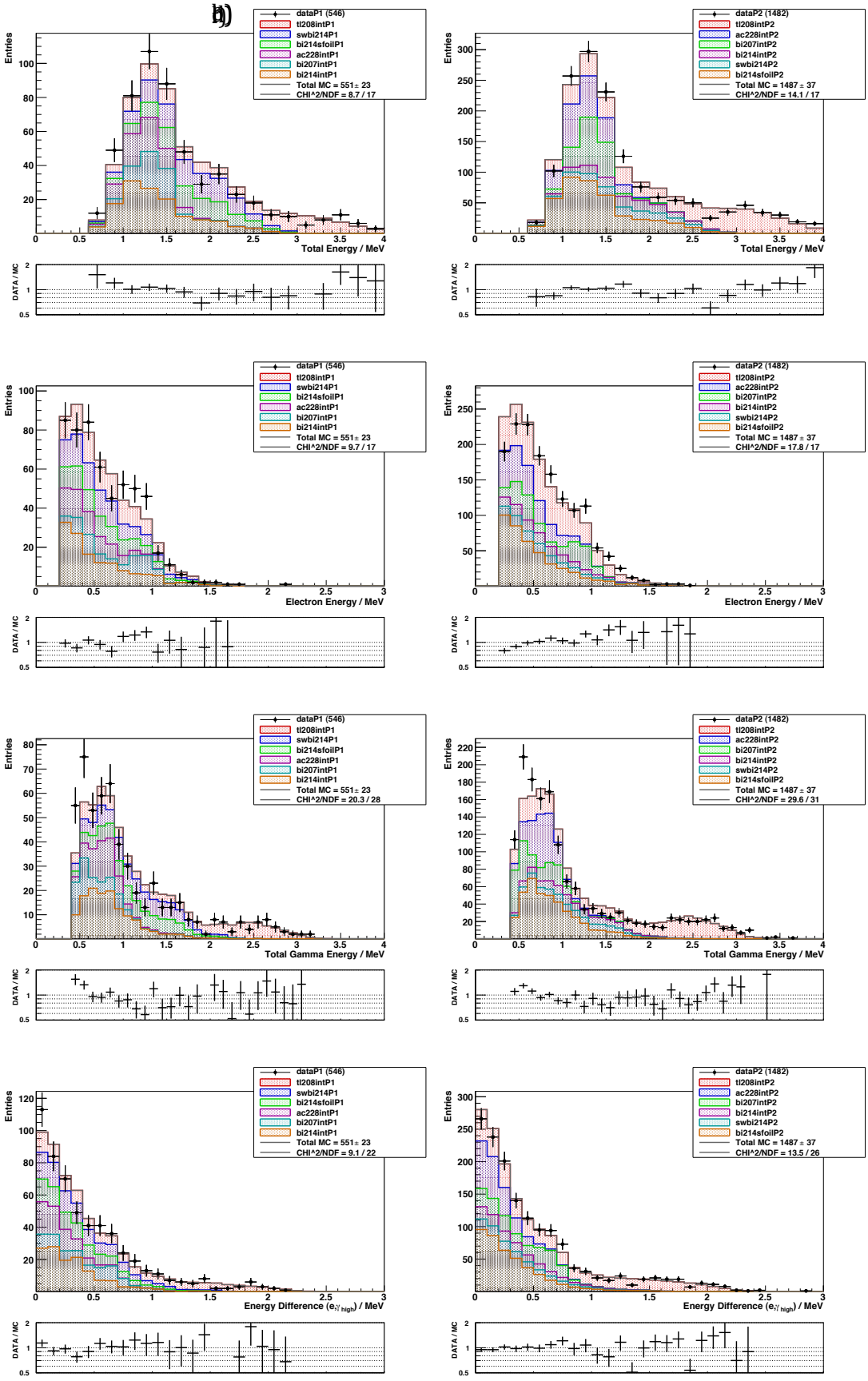

Figure 32 - The distributions of total energy, electron energy, total gamma energy and energy difference between the electron and the more energetic gamma within the 1e2γ topology. a), c), d) and g) are of Phase-1 and b), d) f) and h) are of Phase-2. (see Appendix D for legend key)

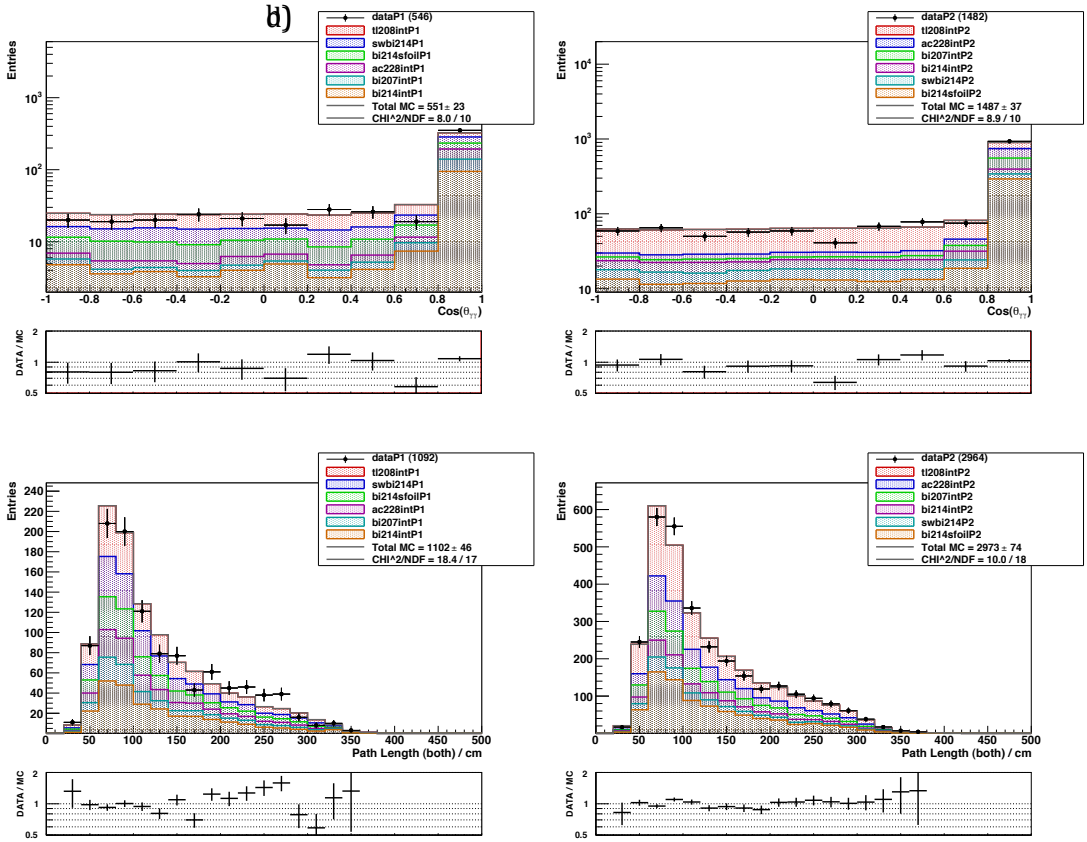

Figure 33 – The distributions of cosine between the two gammas and the path length of both of the gammas within the 1e2γ topology. a) and c) are of Phase-1 and b) and d) are of Phase-2. (see Appendix D for legend key)

Although the 1e2γ topology has the least entries of any internal topology, it is an excellent crosscheck for many internal and external backgrounds as it is affected by many different isotopes and can be examined using many different distributions.

Using the region above an energy of 2.7 MeV in the distributions of the sum of the energy of the γ for Phase-1 and Phase-2, Figure 33.e and Figure 33.f respectively, the activity of Tl-208 within the foil is determined to be 5.5×10^{-3} Bq. It is also found that the earlier defined values for internal Ac-228, Bi-207, Bi-214 and SWIRE Bi-214 agree in both Phase-1 and Phase-2, using all of the distributions shown in Figure 33.a-l.

6.5.6 1e Channel

The 1e topology is used to measure the activity of both internal K-40 and SFOIL Bi-210. Since only one particle is involved in the 1e topology, it is not possible to calculate an

internal or external hypothesis. In order to limit the incursion of external background, events are only selected if:

- the track has negative curvature (negative charge)
- the track vertex is within the Nd-150 foil (see Section 5.3)
- the track has a hit in the first layer of Geiger cells.

In addition to these requirements, the 1e selection also requires the Pa-234m hotspot to be removed and the minimum particle energy to be larger than 0.3 MeV.

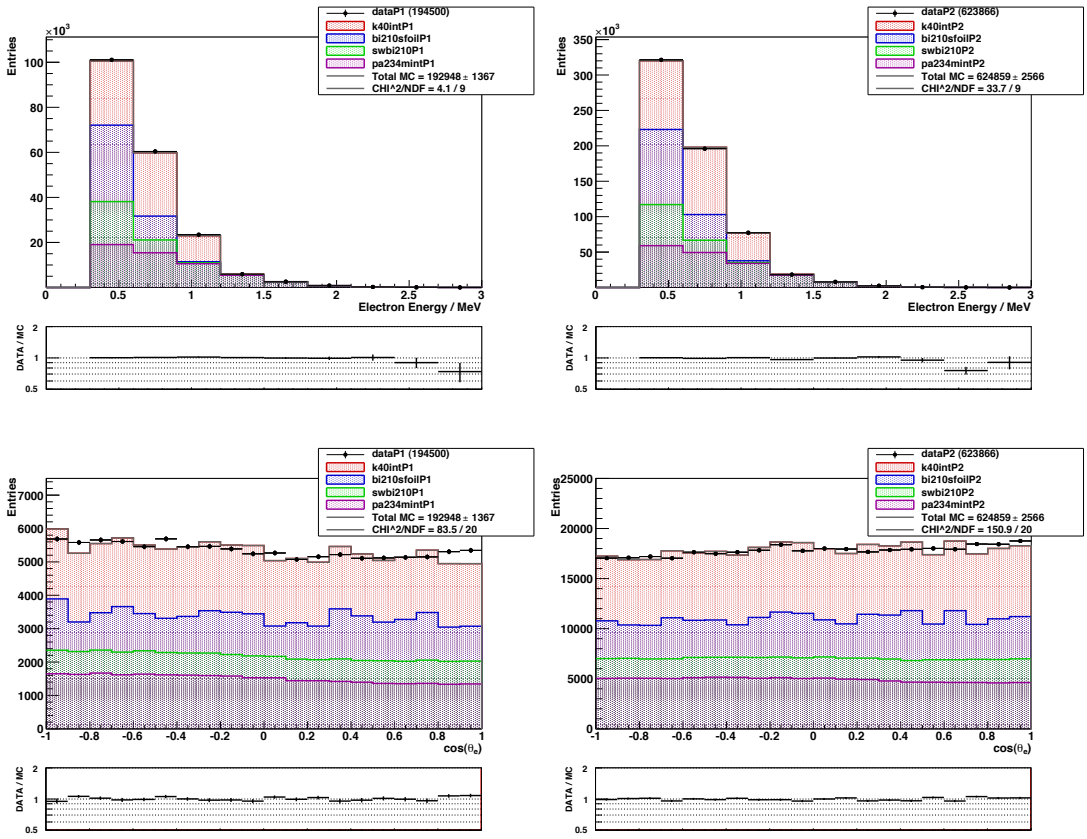

Figure 34 - The 1e topology selection distributions of electron energy and cosine of the electron. Plots a) and c) are of Phase-1 and b) and d) are of Phase-2. (see Appendix D for legend key)

Using both the distributions of electron energy, Figure 34.a and Figure 34.b, and of $\cos(\theta_e)$, Figure 34.c and Figure 34.d the activity of K-40 and Bi-210 is examined. As expected, the determined activity for K-40 internal is constant for both Phase-1 and Phase-2. However, the activity of SFOIL Bi-210 is not constant, but instead of decreasing, the expected change, the activity increases.

The increase in Bi-210 activity on the surface of the foil has three possible causes, the first being that in either Phase-1, Phase-2 or both, the activities of Bi-210 from other physical sources such as on the surface of the wires and the surface of the scintillators is incorrect The second potential cause for this increase is un-simulated Bi-210 from within the foil itself. If the majority of the Bi-210 detected is caused by a constant component of Bi-210 from within the foil, the increase could be contained within a statistical fluctuation. The final potential cause is that the quantity of Pb-210 might have built up within the detector before the installation of the radon facility. The half-life of Pb-210 is 22.3 years for decay by a low energy (Q_β = 61 KeV) into Bi-210. Due to the low energy decay of Pb-210, it cannot be measured within NEMO-3. This cause comes with the clause that the amount of Bi-210 deposited on the surface of the wires, scintillators and other foils should also increase, therefore can be easily shown or refuted within future analysis.

6.6 Selection Efficiency

Events generated in the MC simulations are distributed between every run, weighted by the length of the run; this is described by,

$$N_i = N_{tot} \frac{t_i}{t_{tot}},$$

where N_i and N_{tot} represent the number of generated events for a single run and in total, respectively, t_i and t_{tot} represent the time of a single run and the total running time respectively. From this, the selection efficiency, ε, is calculated by dividing the number of events after selection by the calculated number of events before the selection process.

6.7 Background Summary

Using all of the channels discussed and the global external background model the external backgrounds were determined to be the values seen in Table 7.

Source		Isotope	Activity / Bq		Decay Method
			Phase-1	Phase-2	
Air Under the Iron Shield (EXBG2)		Bi-214	566	0	β-α
		Pb-214	566	0	β
		Tl-208	11.5	0	βγ & βγγ
Iron Shield (EXBG4)		Ac-228	1.35×10^{3}		βγ & βγγ
		Bi-214	7.36×10^{3}		β-α
		Tl-208	484		βγ & βγγ
Internal Tower (EXBG6)		Co-60	29.4	18.4	β
Iron Petals (EXBG7)		Ac-228	8.54		βγ & βγγ
		Bi-214	9.12		β-α
		Co-60	6.09		β
		K-40	100		β
		Pa-234m	1.51×10^{3}		β
		Tl-208	3.07		βγ & βγγ
PMT Shield (EXBG8)		Co-60	23.3	14.6	β
		Pa-234m	3.42×10^{3}		β
PMT Glass (EXBG11)		Ac-228	72.7		βγ & βγγ
		Bi-214	324		β-α
		K-40	1.08×10^{3}		β
		Tl-208	27.0		βγ & βγγ
Copper Above Petals (EXBG17)		Co-60	76.1	47.6	β
Inside Scintillator	SCII	K-40	2.53		β
	SCIO	K-40	4.18		β
	SCIP	K-40	0.464		β
Scintillator Surface (SSCIN)		Bi-210	30.4		β
		Bi-214	0.38		β-α
		Pb-214	0.38		β
Surface of the Foils (SFOIL)		Bi-210	0.99	0.963	β
		Bi-214	18.5×10^{-3}	8.01×10^{-3}	β-α
Surface of the Wires (SWIRE)		Bi-210	9.93	8.192	β
		Bi-214	728×10^{-3}	143×10^{-3}	β-α
		Pb-214	728×10^{-3}	143×10^{-3}	β

Table 7 - The external background model used in the region of the Nd-150 foil.

The homogenous internal backgrounds for the Nd-150 foil are displayed in Table 8.

Isotope	Activity / mBq	Method
Ac-228	1.42	βγ & βγγ
Bi-207	11.5	βγ & βγγ
Bi-212	1.42	βγ & βγγ
Bi-214	0.503	β-α
Eu-152	2.6	βγ
Eu-154	1.24	βγ
K-40	10.3	β
Pa-234m	1.97	β
Pb-214	0.168	β-α
Tl-207	0.55	βγ & βγγ

Table 8 - The homogenous backgrounds contained within the Nd-150 foil.

(7.1)

(7.2)

Chapter 7: Double Beta Decay

The half-life of Nd-150 via the decay of two-neutrino double β decay (2ν2β) can be calculated using the equations;

$$N_{decays}(t) = \varepsilon N_0 \left(1 - \exp\left[-\ln 2\left(\frac{t}{T_{1/2}}\right)\right]\right),$$

$$T_{1/2} = \varepsilon N_0 \ln 2\left(\frac{t}{N_{decays}(t)}\right),$$

where ε represents the efficiency of selection, N_0 is the number of Nd-150 atom within the foil, which is 1.462×10^{23}, and t and $T_{1/2}$ represent the time duration of observation and the half-life of Nd-150, respectively.

7.1 Coincidence Bias

An extra component is required to correct for an observational bias. The NEMO-3 detector is subject to both noise created from the PMTs themselves and coincidences. These coincidences occur when during a double β decay of a Nd-150 nucleus another isotope decays elsewhere within the detector and causes another PMT hit. Therefore

this event is excluded from the 2e topology. This effect is not simulated within the NEMO-3 MC and therefore needs to be corrected for.

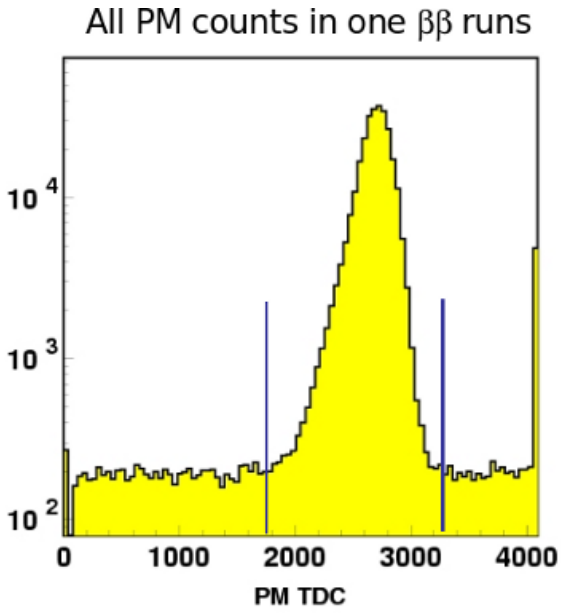

Figure 35 - A distribution of the TDCs recorded from PMT hits using a 2 electron selection. The background rate is observed to be approximately 200, while the peak of true event PMT hits exceeds 30,000.

A study of the Nd-150 foil found this coincidence factor (F) to be 3.6% using Figure 35. The factor is obtained by estimating the number of unrelated PMT hits during an event by observing the number of unrelated events that were during an event, but not in-time with the decay, shown in Figure 35 at the regions excluded from the peak.[28]

The final equation for calculating the half-life is

$$T_{1/2} = \frac{\varepsilon}{F} N_0 \ln 2 \left(\frac{t}{N_{decays}(t)} \right).$$

7.2 Dead Time

The periods used for this analysis are:

- Phase-1 = 29,478,404s
- Phase-2 = 112,011,120s
- Total Time = 141,489,524s.

These times do not represent the true time the detector is able to record events. After detecting an event it is 1.4 ms before the detector is able to detect another event. It is therefore necessary to take this dead time into account. The relative proportion of the total time that is dead time, for each phase is:.

- Fraction of Phase-1 = 0.0161,
    - corrected observational time = 29,003,801s
- Fraction of Phase-2 = 0.0113,
    - corrected observational time = 110,349,995s.[29]

Therefore the corrected total time of observation is 139,353,796s (4.42 years).

7.3 Selection Criteria

The selection criteria are optimised to increase the signal efficiency. The selection is modified compare to the requirements in the previous analysis of Nd-150 with NEMO-3.[26] By studying the MC simulations, it is found that 99.99% of the Nd-150 double β decay signal has at least one electron that struck the first layer of Geiger cells. Events are therefore selected by requiring at least one hit in the first layer, opposed to allowing hits on either of the first two layers.

Nd-150 signal is removed by selecting only events with tracks greater than 30 cm. As the proportion of signal to background in the region track length less than 30 cm is of

the same order as in the region track length greater than 30 cm, these events are not rejected.

The previous analysis of Nd-150 removed events if the track vertices are:

- ΔZ > 4 cm,
- Δϕ > 2 cm/radius,

where ΔZ and Δϕ represent $|Z_1 - Z_2|$ and $|\phi_1 - \phi_2|$ between the two tracks, respectively.[26] Examining the signal-to-background ratio for these distributions, it is found that the proportion of signal remains greater than that of the background until the vertices are separated by:

- ΔZ > 5 cm,
- Δϕ > 2.5 cm/radius.

Taking into account all of these modifications, the final selection criteria for selecting double β decay signal is:

- Exactly two negatively charged particles associated with only two PMT hits
- Both PMT hits must have LEC available
- Both PMTs must have a LEC flag <= 2
- Run status and PMT statuses must be good
- The vertices of the tracks must fall within the Nd-150 foil
    - -117 cm < Z < 117 cm
    - 1.802 radians < Φ< 1.846 radians
- Each track vertex must be within 5 cm of the other, in both dimensions
- Neither track vertex falls within the Pa-234m hotspot region
- Internal TOF selection
- Both corrected energy detections must be greater than 0.2 MeV
- There must be hit on the first layer of Geiger cells

7.4 Measurement of Nd-150 2νββ Half-Life

The final selection criteria are applied to Phase-1 and Phase-2 separately, yielding the event counts, signal over background ratios, efficiencies and half-lives given in Table 9.

Phase	Events			S/B	ε	$A_{2\nu2\beta}(^{150}Nd)$ / μBq	$T_{1/2}$ / years×10^{18}
	Data	Signal	Bkg.				
One	898	647	251	2.58	6.16%	369.9±17.8	$8.68^{+0.44}_{-0.40}$
Two	3448	2535	913	2.78	6.45%	374.7±8.7	$8.57^{+0.21}_{-0.20}$

Table 9 - The results of performing selection and fitting on Phase-1 and 2 separately. The half-lives are shown with statistical error.

By combining the two samples and fitting the Nd-150 signal to the distribution, shown in Figure 36-39, it is possible to use the data of 4.42 years of data collection. The fit after selection yields 4346 events.

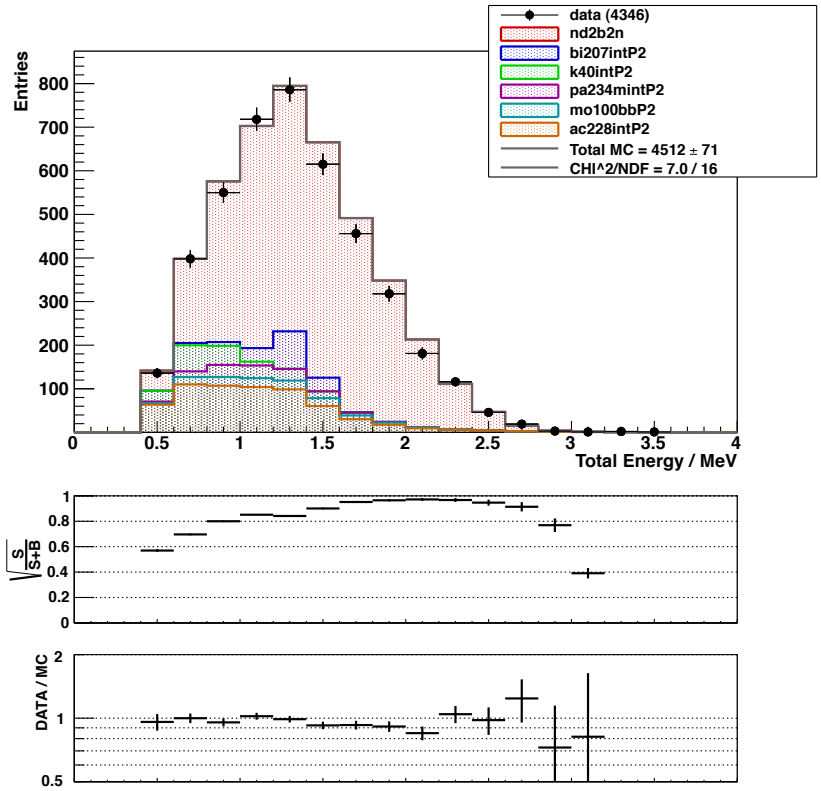

Figure 36 - The total energy distribution of both Phase-1 and Phase-2 data. Fit with 2νββ decay signal for Nd-150, shown in red. (see Appendix D for legend key)

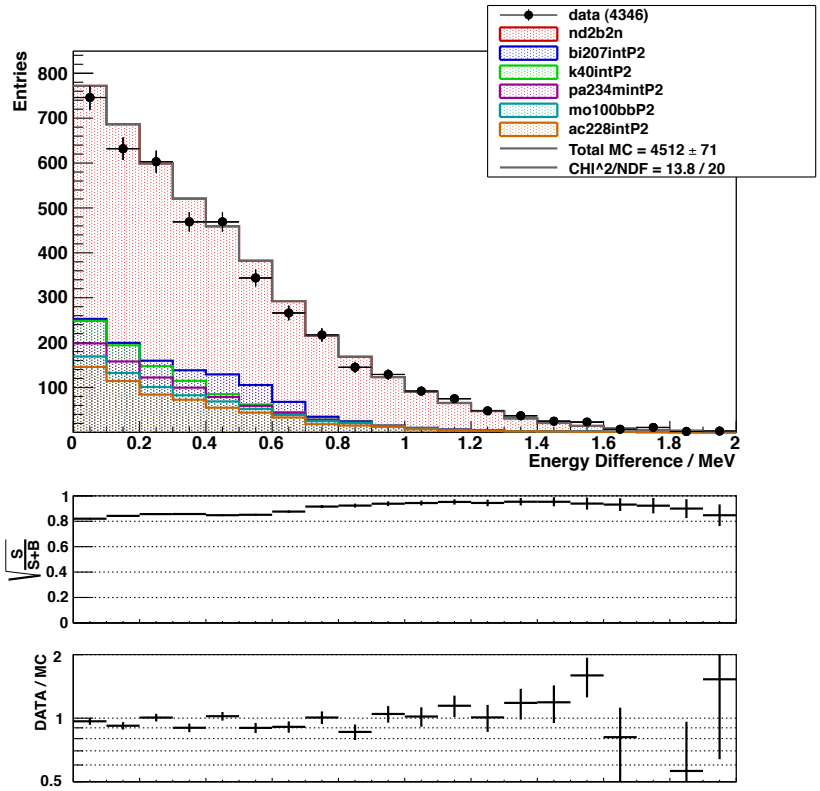

Figure 37 - The energy difference distribution of both Phase-1 and Phase-2 data. Fit with 2νββ decay signal for Nd-150, shown in red. (see Appendix D for legend key)

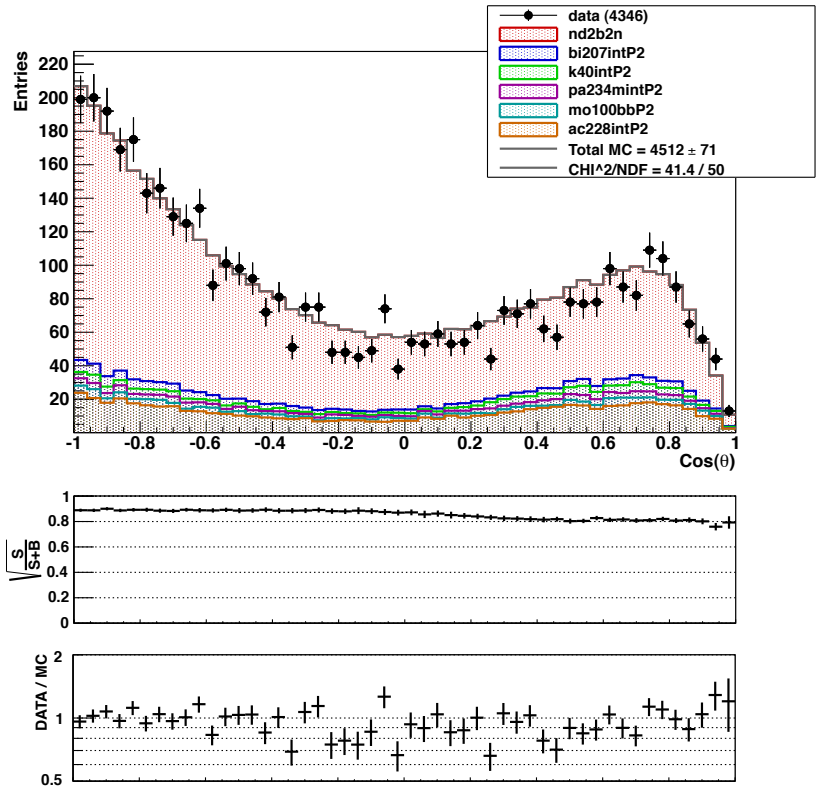

Figure 38 - The cos(θ) distribution of both Phase-1 and Phase-2 data. Fit with 2νββ decay signal for Nd-150, shown in red. (see Appendix D for legend key)

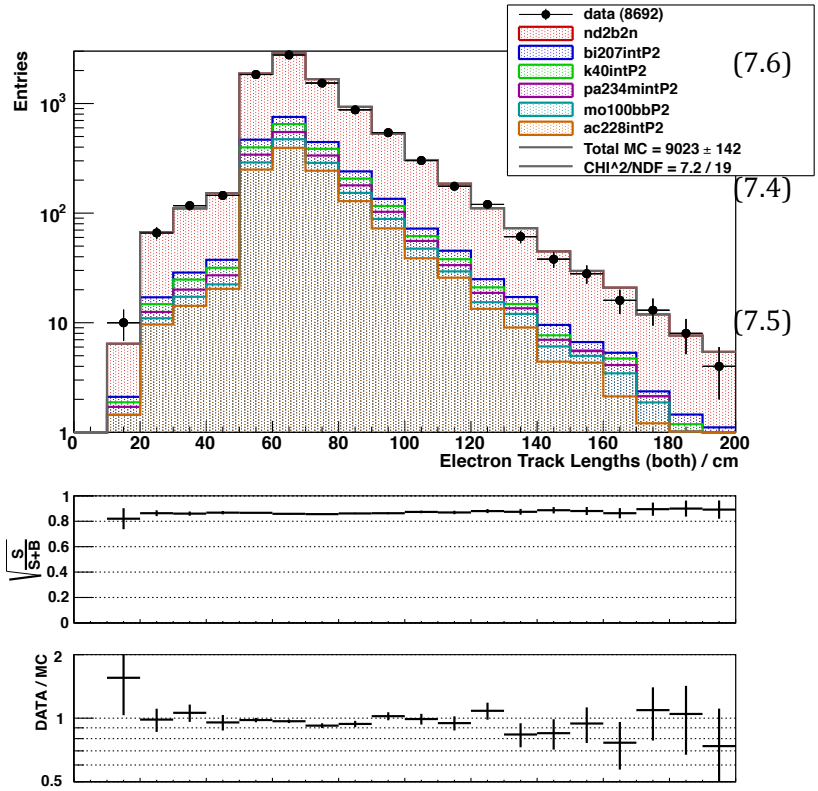

Figure 39 - The track length distribution for both of the electrons using both Phase-1 and Phase-2 data. Fit with 2νββ decay signal for Nd-150, shown in red. (see Appendix D for legend key)

The fitting program within Ana determines there to be 3188±64 signal events within the sample taken, which is an increase of two events from the direct addition of the Phase-1 and Phase-2 results. This increase of two events is considered to be negligibly small. This number of signal events with the selection efficiency of 6.41%, in-conjunction with the observational correction of 3.6%, equates to the values:

$$N_{decayed}(2\beta 2\nu) = 52327 \pm 1100$$

$$T_{1/2} = \left(8.55 \pm 0.18(stat.)\right) \times 10^{18}\ \text{years.}$$

This value is outside of the statistical error of previous half-lives determined using NEMO-3 data and software. But by removing the correction values, derived from coincidence and dead time, the half-life calculated using this fit is

$$T_{1/2} = (9.00 \pm 0.19(stat.)) \times 10^{18}\ \text{years,}$$

(7.7)

which is in agreement with the previously measured half-lives of Nd-150 via double β decay, which is

$$T_{1/2} = (9.11^{+0.25}_{-0.22}(stat.)) \times 10^{18} \text{ years.[26]}$$

The statistical uncertainties of these two half-lives are partially correlated due to overlapping data sets.

7.5 Systematic Uncertainties

The systematic uncertainties of the selection are derived via several techniques:

- By fitting the Nd-150 signal using many different distributions (see Appendix C) it is possible to establish an uncertainty caused by either incorrect activities within the background models or inaccuracies within the simulations. From this an uncertainty of $\pm 0.027 \times 10^{18}$ years is established.
- By comparing the half-lives derived from Phase-1 and Phase-2 individually and combined a deviation of $\pm 0.13 \times 10^{18}$ years is found.
- Altering the external background model to remove the excess seen in the 1e1γ topology, by scaling the backgrounds down produced a systematic uncertainty of $\pm 0.002 \times 10^{18}$ years.
- The final selection is modified by introducing a requirement that removes all events with Geiger hits that are not associated with a track. This selection removes events, in which the tracking algorithm incorrectly reconstructed vertices due to extra Geiger cells firing. This selection has very low statistics and introduces a bias between data and MC and therefore unfit for analysis. But by comparing the Nd-150 signal from these two selections an error of 4.4% is obtained which equates to an error of $\pm 0.37 \times 10^{18}$ years.

Adding these uncertainties in quadrature an overall systematic uncertainty of 0.39×10^{18} years is determined.

(8.1)

(8.2)

Chapter 8: Conclusions

The half-life of Nd-150 via double β decay is determined to be,

$$T_{1/2} = \left(8.55 \pm 0.18(stat.) \pm 0.39(syst.)\right) \times 10^{18} \text{ years.}$$

Although this half life is not in agreement with the previously calculated half life, using a partial NEMO-3 data set, of

$$T_{1/2} = \left(9.11^{+0.25}_{-0.22}(stat.) \pm 0.62(syst.)\right) \times 10^{18} \text{ years,}$$

this can be primarily explained by the inclusion of the scale factors for dead time and coincidence. Due to the inclusion of the full NEMO-3 data set, it was possible to greatly reduce the statistical uncertainties.

Future analysis of the Nd-150 foil has several issues of uncertainty to investigate and potentially reduce. One of these is an investigation into the coincidence correction factor. A second area of further analysis would be to understand the miss-fitting external background model in the 1e1γ topology. Although the uncertainty in the tracking algorithm has been reduced, it still provides the largest aspect of the systematic error. This could be reduced further by the use and comparison of the new tracking algorithm within the NEMO-3 software.

Appendix A – Run Status

Run Status	Description
0	Bad run, do not use it for ββ analysis
1	Good run quality
10	Some PM HV boards or PM acq creates are off
100	Some GG HV boards or GG acq crates are OFF
1000	< 24 hours after calibration run
10000	< 24 hours after general HV shutdown
20000	<24 hours after HV shutdown of 1 HV board
100000	Ventilation OFF high radon rate
1000000	No laser run for day correction
10000000	<24 hours after acquisition crates or electronic shutdown
100000000	Wrong HV for some PM
1000000000	Jump of some PM HV board due to a noisy PM (jump of acquisition rate or acquisition time-off)

Appendix B - Global External Background Model

Source	Isotope	Activity / Bq	
		Phase-1	Phase-2
Air Under the Iron Shield (EXBG2)	Bi-214	566	0
	Pb-214	566	0
	Tl-208	11.5	0
Iron Shield (EXBG4)	Ac-228	1.35×10^{3}	
	Bi-214	7.36×10^{3}	
	Tl-208	484	
Internal Tower (EXBG6)	Co-60	29.4	18.4
Iron Petals (EXBG7)	Ac-228	8.54	
	Bi-214	9.12	
	Co-60	6.09	
	K-40	100	
	Pa-234m	1.51×10^{3}	
	Tl-208	3.07	
PMT Shield (EXBG8)	Co-60	23.3	14.6
	Pa-234m	3.42×10^{3}	
PMT Glass (EXBG11)	Ac-228	72.7	
	Bi-214	324	
	K-40	1.08×10^{3}	
	Tl-208	27.0	
Copper Above Petals (EXBG17)	Co-60	76.1	47.6
Inside Scintillator (SCI)	K-40	7.17	
Scintillator Surface (SSCIN)	Bi-210	30.4	
	Bi-214	0.38	
	Pb-214	0.38	
Surface of the Wires (SWIRE)	Bi-210	9.93	8.192
	Bi-214	1.21	192×10^{-3}
	Pb-214	1.21	192×10^{-3}

Appendix C – Systematic Uncertainties

Distribution	Fitting Range	Half-life / years×10^{18}
Total Energy	0.4 – 3.0 MeV	8.554
Energy Difference	0.0 – 2.0 MeV	8.557
Electron Energy (Both)	0.2 – 2.0 MeV	8.569
Electron Energy (High)	0.2 – 2.0 MeV	8.581
Electron Energy (Low)	0.2 – 1.2 MeV	8.564
Cosine	-1.0 – 1.0	8.557
Track Length (Both)	20 – 180 cm	8.562
Track Length (Long)	30 – 180 cm	8.566
Track Length (Short)	10 – 110 cm	8.570

Appendix D – Legend Key

The legend code is a collection of information, about the radioactive sources, produced by Ana. The suffixes P1 and P2 denote the phase of the sample. If neither of these suffixes are present the sample is of both phases.

Legend Code	Location	Isotope/Decay Mode
mo100bb	Neighbouring Mo-100 Foil	2νββ
nd2b2n	Nd-150 Foil	2νββ
ca48y90	Ca-48 Foil	Y-90
paex7	Iron Petals	Pa-234m
biex11	PMT Glass	Bi-214
swbi214	Surface of the Wires	Bi-214
bi214sfoil	Surface of the Foils	Bi-214
bi214int	Nd-150 Foil	Bi-214
bi214ss	Surface of the Scintillators	Bi-214
zr96bi214	Zr-96 Foil	Bi-214
mo100bi214	Neighbouring Mo-100 Foil	Bi-214
biex2	Air Under the Iron Shield	Bi-214
biex4	Iron Shield	Bi-214
kex11	PMT Glass	K-40
coex8	PMT Shield	Co-60
tlex4	Iron Shield	Tl-208
bi210ss	Surface of the Scintillator	Bi-210
bi207int	Nd-150 Foil	Bi-207
ac228int	Nd-150 Foil	Ac-228
tl208int	Nd-150 Foil	Tl-208
k40int	Nd-150 Foil	K-40
bi210sfoil	Surface of the Foils	Bi-210
swbi210	Surface of the Wires	Bi210
pa234mint	Nd-150 Foil	Pa-234m

References

[1] L.M. Brown. The idea of the neutrino. Phys. Today, 31:23, 1978.

[2] W. R. Kropp, J. Schultz and H. W. Sobel, "1998, University of California: In Memoriam," 2012 (05/08), (1998).

[3] J. N. Bahcall and MH Pinsonneault, "Standard solar models, with and without helium diffusion, and the solar neutrino problem," Reviews of Modern Physics 64 (4), 885 (1992).

[4] Q. Ahmad et al. [SNO Collaboration]. Direct evidence for neutrino flavor transformation from neutral-current interactions in the Sudbury neutrino observatory. Phys. Rev. Lett., 89:011301, 2002.

[5] B. Kayser. Neutrino mass, mixing and flavour change. arXiv:hep-ph/0211134v1, 2002.

[6] P. Higgs. Spontaneous symmetry breakdown without massless bosons. Phys. Rev., 145:1156, 1966.

[7] Tobias Koettig, "Neutrinoless Double Beta Decay," 2012 (05/08).

[8] Q. Ahmad et al. [SNO Collaboration]. Direct evidence for neutrino flavor transformation from neutral-current interactions in the Sudbury neutrino observatory. Phys. Rev. Lett., 89:011301, 2002.

[9] Z. Maki, M. Nakagawa and S. Sakata. Remarks on the unified model of elementary particles. Prog. Theor. Phys., 28:870, 1962.

[10] F. Feruglio, A. Strumia and F. Vissani. Neutrino oscillations signals in β and 0νββ experiments. Nucl. Phys., B637:345, 2002.

[11]S. Abe et al. [KamLand Collaboration]. Precision measurement of neutrino oscilattions parameters with KamLand. *Phys. Rev. Lett.,* 100:221803, 2008

[12] W. Furry. On transition probabilities in double beta-disintegration. Phys. Rev., 56:1184, 1939

[13] M. Doi, T. Kotani, and E. Takasugi. Double beta decay and Majorana neutrino. *Prog. Theor. Phys. Supp.,* 83:1, 1985

[14] R. Arnold, C. Augier, A.M. Bakalyarov, J. Baker, A. Barabash, et al. Technical design and performance of the NEMO 3 detector. Nucl.Instrum.Meth., A536:79–122, 2005.

[15] T. Lamhamdi. Double decay study of ^{150}Nd. NEMO 3 internal note, 2007.

[16] D. Alburger and A. Sunyar. Decay of Bi-207. Phys. Rev., 99:695, 1959.

[17] V. Tretyak. Laser energy corrections for the year 2010. NEMO-3 internal note, *NemoDocDB-doc-1686-v1.* June 2011.

[18] V. Kovalenko. Laser time corrections (LTCs) for NEMO 3 data. NEMO 3. internal note, 2006.

[19] V. Tretyak. The nemo3 results after completion of the data taking. MEDEX 2011, 2011.

[20] V. Tretyak. Use of PM and RUN statuses. NEMO 3. internal note, 2006.

[21] O. A. Ponkratenko, V. I. Tretyak, and Yu. G. Zdesenko. The Event generator DECAY4 for simulation of double beta processes and decay of radioactive nuclei. Phys. Atom. Nucl., 63:1282–1287, 2000.

[23] J. Argyriades et al. Measurement of the background in the NEMO 3 double beta decay experiment. Nucl. Instrum. Meth., A606:449–465, 2009.

[24] C. Hugon. Final status of the Time Of Flight in NAT++. internal note, *NemoDocDB-doc-2094-v2.* 2012.

[25] K. Yamazaki. Measurement of the Two Neutrino Double Beta Decay Half-life of 150Nd with the NEMO-3 Detector. MSc thesis, University of Manchester, 2011

[26] Nasim Fatemi-Ghomi. Measurement of the double beta decay half-life of Nd-150 and search for neutrinoless decay modes with NEMO-3 detector. PhD thesis, University of Manchester, 2009.

[27] V. Tretyak. External Background. internal note, *NemoDocDB-doc-662-v1*. 2009

[28] S. Blondel. ^{150}Nd Analysis. internal note, *NemoDocDB-doc-2359-v3*. 2012

[29] V. Tretyak. Search for 0νββ decay of Mo100 and Se82 with data of the year 2010. internal note, *NemoDocDB-doc-1490-v1*. 2011